POLIPHON conversion factors for retrieving dust-related cloud condensation nuclei and ice-nucleating particle concentration profiles at oceanic sites

Yun He[1,2,3,*], Zhenping Yin[4,*], Albert Ansmann[5], Fuchao Liu[1,2,3], Longlong Wang[4], Dongzhe Jing[1,2,3],
5   Huijia Shen[1]

[1]School of Electronic Information, Wuhan University, Wuhan, China
[2] Key Laboratory of Geospace Environment and Geodesy, Ministry of Education, Wuhan, China
[3]State Observatory for Atmospheric Remote Sensing, Wuhan, China.
[4]School of Remote Sensing and Information Engineering, Wuhan University, Wuhan, China.
10   [5]Leibniz Institute for Tropospheric Research, Leipzig, Germany

Correspondence to: Yun He (heyun@whu.edu.cn), Zhenping Yin (zp.yin@whu.edu.cn)

Abstract. Aerosol-Cloud interactions (ACI) result in the largest uncertainties in the global radiation budget so far. To improve the current consideration of ACI in global circulation models, it is necessary to characterize the 3-D distribution of

15   dust-related Cloud Condensation Nuclei Concentration (CCNC) and Ice Nucleating Particle Concentration (INPC) globally. This can potentially be realized using the POLIPHON (POlarization LIdar PHOtometer Networking) method together with spaceborne lidar observations. However, dust-related conversion factors to convert bulk aerosol optical properties from lidar measurements to aerosol microphysical properties, are still less constrained in many regions, which limits the applications of POLIPHON method. Here we retrieve the essential dust-related conversion factors at the remote oceanic/coast sites using the

20   historical AERONET (AErosol RObotic NETwork) databases. Depolarization-ratio-based dust ratios R_d at 1020 nm are applied to identify the dust-occurring cases so that it can be possible to contain fine-mode dust dominated cases (after the preferential removal of large-size dust particles during transport), study the evolution of dust microphysical properties along the transoceanic pathway, and mitigate occasional interference of large-size marine aerosols. The newly proposed scheme is proven to be valid and feasible by intercomparisons with previous studies at nine sites in/near the deserts. The dust-related

25   conversion factors are calculated at 20 oceanic/coast sites using both PD (pure dust) and PD+DDM (dust-dominated mixture) datasets. At nearly half sites, the conversion factors are solely calculated using the PD data sets; while at the rest sites, the participation of DDM datasets is required to ensure enough data points in the calculation. Evident variation trends in conversion factors are found for $c_{v,d}$ (extinction-to-volume, gradually decrease), $c_{250,d}$ (extinction-to-particle (with radius >250nm) number concentration, gradually increase) and $c_{s,d}$ (extinction-to-surface area concentration, plunge of

30   decrease) along both the transpacific and transatlantic dust transport pathways. The retrieved dust-related conversion factors are anticipated in inversing 3-D dust-related CCNC and INPC distribution globally to improve the understanding of ACI in atmospheric circulation models.

1 Introduction

35   Clouds are widely present in the Earth's atmosphere, covering approximately 2/3 of the Earth's surface. They play an essential role in weather, hydrology, climate, air chemistry, and several practical applications (Spänkuch et al., 2022). Clouds modify the radiation budget of the Earth by governing the incoming solar radiation and outgoing longwave radiation, thus significantly affecting the global climate. The level of induced net radiation is closely associated with the microphysical characteristics of cloud particles (either cloud drops or ice crystals), i.e., size, concentration, phase, shape, and so on, which

40   are greatly influenced by aerosol-cloud interactions (ACI), also known as 'aerosol indirect effects', resulting in the largest uncertainties in the global radiation budget so far (IPCC, 2013; Rosenfeld et al., 2014).

    For liquid-water clouds, aerosols serve as cloud condensation nuclei (CCN) to alter the drop size and albedo (Twomey, 1974) as well as to postpone the initiation of rainfall and increase the lifetime and coverage of clouds (Albrecht, 1989). For mixed-phase and ice clouds, heterogeneous nucleation is another crucial effect in which proper aerosol particles may act as

45   ice-nucleating particles (INP) to trigger the in-cloud ice formation (from either vapor or liquid water) (Ansmann et al., 2019a, 2019b, 2021; Murray et al., 2012; Cziczo et al., 2013; Yin et al., 2021). In the ACI study, it is of great importance to quantify the number concentration of CCN and INP. In recent years, aerosol optical depth (AOD) and aerosol index (AI) are evaluated to be not accurate enough to serve as CCN proxies (Shinozuka et al., 2015; Stier, 2016), thus motivating the scientific community to estimate CCN concentration (CCNC) (Mamouri and Ansmann, 2016; Choudhury and Tesche, 2022;

50   Patel et al., 2022; Lenhardt et al., 2022). INP concentrations (INPC) are also estimated in many studies to conjecture the initial in-cloud ice crystal number concentration (ICNC) via primary heterogeneous nucleation (Ansmann et al., 2019a; He et al., 2022a). Besides, the constraint of ambient INPC can promote an accurate representation of cloud microphysical processes and reduce the uncertainties in estimating the climate feedback associated with ice and mixed-phase clouds in climate models (Li et al., 2022).

55   To estimate the CCNC and INPC, POLIPHON (POlarization LIdar PHOtometer Networking) method was developed by Ansmann et al. (2012) and has been improved for years in several field campaigns (Mamouri and Ansmann, 2014, 2015, 2016, 2017; Marinou et al., 2019). As a remote sensing approach, it has been well verified through comparisons with simultaneous in-situ measurements (Marinou et al., 2019; Wieder et al., 2022); hence, it is applicable for the analysis of long-term observations. In the POLIPHON method, the lidar-derived aerosol extinction coefficient profiles are first divided

60   into the respective contribution from different aerosol types (Tesche et al., 2009; Mamouri and Ansmann, 2016, 2017). Then, these aerosol-type-dependent extinction coefficient profiles are converted into CCNC and INPC profiles by employing the photometer-data-derived conversion factors and different CCN and INP parameterizations. Conversion factors connect the lidar-retrieved aerosol optical properties and aerosol microphysical properties and thus can be used to estimate CCNC and INPC straightforwardly.

65   Dust aerosol is the most abundant aerosol type by mass in the atmosphere (Kok et al., 2021a) and is considered both effective CCN and INP (Mamouri and Ansmann, 2016; He et al., 2021a, 2021b, 2022a, 2022b; Murray et al., 2012; Kanji et al., 2017). Therefore, dust-related CCNC and INPC estimations should be especially focused on. Numerous field campaigns have been conducted to study the regional CCNC and INPC profiles (Haarig et al., 2019; Hofer et al., 2020; Engelmann et al., 2021; He et al., 2021b). Benefiting from the spaceborne lidar, e.g., CALIOP (Cloud-Aerosol Lidar with Orthogonal

70   Polarization) launched in April 2006 (Winker et al., 2007) and EarthCARE mission in progress (Illingworth et al., 2015), it allows us to characterize the 3-D distribution of dust-related CCNC and INPC at a global scale and in turn to improve the current consideration of ACIs in global circulation models (Mamouri and Ansmann, 2015; Froyd et al., 2022).

To do this, the first challenge is to retrieve the global dust-related conversion factors. However, they are generally regional-dependent and relevant to the microphysical properties of dust particles. Mamouri and Ansmann (2015) first

75   calculated the dust-related conversion factors based on the sun/sky photometer data during several field campaigns, including SAMUM-1 (Saharan Mineral Dust Experiment), SAMUM-2, and SALTRACE (Saharan Aerosol Long-range Transport and Aerosol–Cloud Interaction Experiment) and long-term observations in Limassol. Subsequently, Ansmann et al. (2019b) obtained the dust-related conversion factors using AERONET (AErosol Robotic NETwork) data at the typical sites near the main deserts. They assumed the predominate contribution of dust in the atmospheric column and systematically

80   applied the column-integrated Ångström exponent (AE for 440–870nm) < 0.3 and AOD at 532nm > 0.1 as the criteria in selecting dust presence cases. However, there are still many gaps in the downstream areas along dust transport pathways due to insufficient data points fulfilling the criteria. Besides, the Ångström-exponent-based dust selection scheme may exclude a part of fine-mode dust particles, resulting in a potential deviation in the conversion factors. The two major gaps are the remote oceans and those polluted city regions (He et al., 2019b; Zhang et al., 2022). The ocean areas are less affected by

85   complicated anthropogenic aerosols and may always be intruded by long-range transoceanic dust plumes (Yu et al., 2021; Dai et al., 2022), which are thus preferentially focused on in this study.

To retrieve the dust-related conversion factors at the oceanic/coast sites, we plan to adopt another scheme to select data points, which are representative of dust presence from AERONET databases. The new scheme is based on the particle linear polarization ratio in AERONET Version 3 aerosol inversion product, which is considered a better indicator for non-spherical

90   dust particles (Shin et al., 2018, 2019). Three factors motivate us to do so rather than to use the method raised by Ansmann et al. (2019b). First, applying AE <0.3 to select the dust-occurring data may somewhat exclude some data points representative of fine-mode dust particles that are proven to be present and cannot be ignored (Mamouri and Ansmann, 2014; Shin et al., 2019). Second, tracing the variations in dust-related conversion factors at different oceanic/coast sites may provide us with more information on the evolution of dust microphysical properties along with transoceanic transport routes

95   (Rittmeister et al., 2017). In addition, marine aerosols that mainly consist of sea spray aerosols may occasionally show small AE, which may confuse dust identification by using AE< 0.3 as a criterion (Smirnov et al., 2011; Yin et al., 2019).

In this study, we estimate the dust-related conversion factors in the POLIPHON method at those remote oceanic/coast sites using the AERONET databases, which is considered an important step pushing forward to the study on dust

INPC/CCNC at a global scale and subsequent dust-induced ACI. The paper is organized as follows. We first briefly

100   introduce the POLIPHON method and dust-related conversion factors as well as the AERONET data and dust data
identification scheme. In section 3, we compare the dust-related conversion factor at the sites near deserts with a previous
study, represent the dust-related conversion factors at the ocean and coast sites, and discuss the possible reason behind the
variation in conversion factors along the transoceanic transport. In the last section, summaries and conclusions are given.

2 Data and methodology

2.1 POLIPHON method and conversion factors

105

The POLIPHON method is able to retrieve the height profiles of particle microphysical properties (i.e., particle number,
surface area, and volume concentration) and then, the height profiles of particle mass, CCN, and INP concentration for
several aerosol types using the combination of polarization lidar and sun photometer (Mamouri and Ansmann, 2014, 2015,
2016; Marinou et al., 2019). It has been widely used in the estimations of CCN- and INP-relevant aerosol parameters for the

110   aerosol types including dust (Ansmann et al., 2019a; Hofer et al., 2020; He et al., 2021b, 2022a, 2022b), marine aerosol
(Mamouri and Ansmann, 2016, 2017; Haarig et al., 2019), continental aerosol (Mamouri and Ansmann, 2016, 2017), smoke
(Ansmann et al., 2021; Haarig et al., 2019). In this study, we focus on the dust-related CCN- and INP properties.

In detail, the calculation has been given in Table 1. First, the dust backscatter β_d and extinction α_d coefficient can be
derived by polarization lidar observations based on the inversion method from Fernald (1984) and the dust-component

115   separation method from Tesche et al. (2009) as shown by the following equation:

$$\beta_d(z) = \beta_p(z) \frac{(\delta_p(z) - \delta_{nd})(1 + \delta_d)}{(\delta_d - \delta_{nd})(1 + \delta_p(z))} \tag{1}$$

where $\delta_d = 0.31$ and $\delta_{nd} = 0.05$ are dust and non-dust particle depolarization; δ_p and β_p are the lidar-derived particle
depolarization ratio and backscatter coefficient, respectively. The lidar ratio for dust usually ranges from 30 sr to 60 sr
depending on the different dust sources (Müller et al., 2007; Mamouri et al., 2013; Hu et al., 2020; Peng et al., 2021). Then,

120   the dust extinction coefficient can be converted into particle mass concentration M_d, particle number concentration $n_{250,d}$
(r>250 nm) and $n_{100,d}$ (r>100 nm), and particle surface concentration s_d and $s_{100,d}$ (r>100 nm) by multiplying their
corresponding conversion factors, i.e., $c_{v,d}$, $c_{250,d}$, $c_{s,d}$, and $c_{s,100,d}$. Finally, the dust-related INP concentration $n_{INP,d}$ can be
retrieved by inputting $n_{250,d}$ and S_d into different INP parameterization schemes (DeMott et al., 2010, 2015; Niemand et al.,
2012; Steinke et al. 2015; Ullrich et al., 2017). In addition, $n_{100,d}$ is considered a good proxy for dust-related CCN

125   concentration $n_{CCN,ss,d}$ as discussed by Mamouri and Ansmann (2016). Thus, $n_{CCN,ss,d}$ can be obtained by multiplying $n_{100,d}$
by a water supersaturation-dependent factor $f_{ss,d}$, which is 1.0 for a typical liquid-water supersaturation value of 0.2%.

In the POLIPHON method, as introduced above, a series of conversion factors are essential to the conversion from the
dust extinction coefficient to dust microphysical parameters regarding CCN and INP concentrations. The conversion factors

are pre-calibrated from the historical database of sun photometer observations (denoted as j for each data point, counting
130   from 1 to J_d). The calculation processes are shown below (Ansmann et al., 2019b):

$$c_{v,d} = \frac{1}{J_d} \sum_{j=1}^{J_d} \frac{V_{d,j}/D}{\tau_j/D} = \frac{1}{J_d} \sum_{j=1}^{J_d} \frac{v_{d,j}}{\alpha_{d,j}} \qquad (2)$$

$$c_{250,d} = \frac{1}{J_d} \sum_{j=1}^{J_d} \frac{N_{250,j}/D}{\tau_j/D} = \frac{1}{J_d} \sum_{j=1}^{J_d} \frac{n_{250,d,j}}{\alpha_{d,j}} \qquad (3)$$

$$c_{s,d} = \frac{1}{J_d} \sum_{j=1}^{J_d} \frac{S_j/D}{\tau_j/D} = \frac{1}{J_d} \sum_{j=1}^{J_d} \frac{s_{d,j}}{\alpha_{d,j}} \qquad (4)$$

$$c_{s,100,d} = \frac{1}{J_d} \sum_{j=1}^{J_d} \frac{S_{100,j}/D}{\tau_j/D} = \frac{1}{J_d} \sum_{j=1}^{J_d} \frac{s_{100,d,j}}{\alpha_{d,j}} \qquad (5)$$

135   where D is an introduced thickness for a given aerosol layer and τ is the sun-photometer-measured aerosol optical depth at
500 nm. V_d and N_{250} are the column particle volume concentration and column large particle (radius >250 nm) number
concentration, respectively; S and S_{100} (radius >100 nm) are the column particle surface area concentrations. V_d, N_{250}, S, and
S_{100} are derived from the particle size distribution data in AERONRT aerosol inversion products, which are introduced in
detail in section 2.2. α_d is the layer-mean aerosol extinction coefficient at 550 nm; v_d and $n_{250,d}$ are the layer-mean volume
140   concentration and large particle (radius >250 nm) number concentration, respectively; s_d and $s_{100,d}$ (radius >100 nm) are the
layer-mean particle surface area concentrations. The subscript 'd' denotes 'dust', which is considered the major contribution
in column aerosol loading for the selected sun photometer data.

In addition, it is considered that the estimation of CCN concentration is a challenging task since the ability of aerosol
particles to serve as CCN is complicatedly related to the particle hygroscopicity (associated with particle size and chemical
145   composition) and water supersaturation level (Wang et al., 2010; Moore et al., 2012). As suggested by Shinozuka et al.
(2015), a log-log regression analysis was performed to retrieve the CCN-relevant conversion factor $c_{100,d}$ with the following
equation:

$$\log(n_{100,d}) = \log(c_{100,d}) + \chi_d \log(\alpha_d) \qquad (6)$$

In general, dust-related conversion factors have a regional-dependent characteristic, associated with the origin of dust
150   regions as well as the specific local anthropogenic dust emissions (Philip et al., 2017). To extend the POLIPHON method
towards global dust applications, Ansmann et al. (2019b) provided the dust-related conversion factors at 20 AERONET sites
in/near the typical desert regions, where other types of aerosols contribute less or even negligible to the aerosol properties of
the atmospheric column. Therefore, the obtained conversion factors can be considered the representatives of pure or quasi-
pure dust situations. To pick out the dust-occurring datasets for calculation, they adopted the constraints of column-
155   integrated Ångström exponent (for 440–870nm) <0.3 and aerosol optical depth (at 532nm) >0.1. Due to the influence of

anthropogenic aerosols, dust-occurring data points available are insufficient for calculating the conversion factors. To solve this issue, He et al. (2021b) applied the simultaneous polarization lidar observation to assist the filtration of dust-occurring datasets in Wuhan (30.5N, 114.4E), a central Chinese megacity impacted by both local anthropogenic aerosol emissions and long-range transported dust (He and Yi, 2015; He et al., 2022c; Liu et al., 2022).

160   Dust plumes can also realize transoceanic transport in the Northern Hemisphere; there are two well-known pathways, i.e., the transatlantic route from the Saharan desert to America (Yu et al., 2021; Dai et al., 2022) and the transpacific route from Asian dust sources (Taklimakan Desert and Gobi) to America (Guo et al., 2017; Hu et al., 2019). However, dust-related conversion factors over the ocean are rarely reported. Sea spray aerosols usually have a large size, presenting a similar small Ångström exponent as dust particles (Haarig et al., 2017). To avoid the interference of sea spray aerosol, we here use another

165   scheme to identify the dust-occurring datasets, taking advantage of the particle linear depolarization ratio (PLDR) in AERONET aerosol inversion products (Shin et al. 2019). Therefore, sufficient available dust data points can be picked out even at those remote oceanic sites.

2.2 AERONET data and depolarization-ratio-based dust data points selection

AERONET is a global ground-based aerosol monitoring network and has provided more than 25 years of aerosol column

170   property observations. The employed CE-318 sun-sky photometers allow the direct measurements of solar irradiance generally at 340, 380, 440, 500, 675, 870, 1020, and 1640 nm and directional sky radiance to retrieve the spectral-resolved AODs, and in turn, the additional aerosol inversion products. Moreover, the latest applied CE318-T can also perform nighttime measurements of the spectral lunar irradiance. In this study, the AERONRT database (Holben et al., 1998; Dubovik et al., 2000; Dubovik and King, 2000) was employed in retrieving the dust-related conversion factor at 9 sites

175   near/in the deserts (to compare with the values given in Ansmann et al. (2019b), as a validation of newly-proposed dust selection scheme) and at 20 oceanic/coast sites influenced by long-range transported dust (see figure 1). The oceanic/coast sites can be classified into five regional clusters, i.e., Pacific, Pacific coast, Atlantic, Indian Ocean, and Arctic Ocean, representing dust characteristics in different regions.

We used the quality-assured level-2.0 AOD at 500 nm in AERONET Version 3 aerosol optical depth-solar products (Giles

180   et al., 2019). Moreover, the particle volume size distribution with 22 size bins (radius) ranging from 50 nm to 15 μm and PLDR in AERONET Version 3 aerosol inversion products are also used for calculating V_d, N_{250}, S, and S_{100} as described in section 2.1 (Sinyuk et al., 2020). The specific calculation processes can be found in Mamouri and Ansmann (2015) and Ansmann et al. (2019b). For the near/in desert sites, level-2.0 (quality-assured) aerosol inversion products are applied; while, for the oceanic/coast sites, level-1.5 (cloud-screened and quality-controlled) aerosol inversion products are applied since the

185   level-2.0 PLDR data are unavailable. The basic information of the selected sites is shown in Table 2, including period, longitude, latitude, and the number of data points for total, dust-dominated mixture, and pure dust.

In the AERONET retrieval, based on the aerosol spheroid model, the combination of the particle size distribution and complex refractive index can be used to further compute the two elements of the Müller scattering matrix, i.e., $F_{11}(\lambda)$ and

$F_{22}(\lambda)$ (Bohren and Huffman, 1983; Dubovik et al., 2006; Shin et al., 2018), which can then be used to derive the

190   backscattering PLDR with the following formula:

$$\delta_{\lambda}^{\text{p}} = \frac{1 - F_{22}(\lambda, 180°)/F_{11}(\lambda, 180°)}{1 + F_{22}(\lambda, 180°)/F_{11}(\lambda, 180°)} \quad (7)$$

AERONET PLDR data is a good indicator of dust occurrence, which has been verified to be well correlated with lidar-derived values (Noh et al., 2017). Shin et al. (2018) found that PLDR values at 870 and 1020 nm are more reliable according to the comparison with those from lidar observations for pure dust particles. Therefore, we here use PLDR at 1020 nm δ_{1020}^{p}

195   (only denote as 'PLDR' hereafter) to pick out the dust-occurring data points for POLIPHON conversion factor calculation (Shin et al., 2019). Note that the overestimation of near-infrared PLDR is reported by comparing with concurrent polarization lidar observations (Toledano et al., 2019; Haarig et al., 2022), possibly attributing to the assumption of spheroid particle in AERONET inversion. Nevertheless, δ_{1020}^{p} values are only used to qualitatively identify the dust presence with the presupposed threshold values. Its validity will be verified by comparing the derived conversion factors with those from

200   Ansmann et al. (2019b) in Section 3.1.

To represent the contribution of dust component to the total particle backscatter, it is defined as a variable, column-integrated dust ratio ($R_{\text{d},1020}$) as below:

$$R_{\text{d},1020} = \frac{\left(\delta_{1020}^{\text{p}} - \delta_{\text{nd}}^{\text{p}}\right)\left(1 + \delta_{\text{d}}^{\text{p}}\right)}{\left(\delta_{\text{d}}^{\text{p}} - \delta_{\text{nd}}^{\text{p}}\right)\left(1 + \delta_{1020}^{\text{p}}\right)} \quad (8)$$

It should be noted that the dust ($\delta_{\text{d}}^{\text{p}}$) and non-dust ($\delta_{\text{nd}}^{\text{p}}$) particle depolarization ratios are set to be 0.30 and 0.02, respectively,

205   to be consistent with the value proposed by Shin et al. (2019). These two values are slightly different from those used in the POLIPHON method in Eq. (1). According to the scheme from Shin et al. (2019), we classify data points with $R_{\text{d},1020}$ values of >0.89 as pure dust (PD) and 0.53-0.89 as dust-dominated mixture (DDM, also can be considered 'mixed dust' as in He et al. (2019b). Note that in this study DDM includes the combination of the sectors B (FMF=0–0.4), C (FMF=0.4–0.6), and E (FMF=0.6–1.0) in Shin et al. (2019). A flow chart is given as seen in figure 2. For the near/in desert sites, we presented the

210   results from the PD cluster, which is adequate to calibrate the conversion factors; whilst, for the oceanic/coast sites, the results from both the PD and PD+DDM clusters are provided for comparison.

3 Dust-related conversion factors from the AERONET database

3.1 Intercomparison of dust-related conversion factors near deserts with retrievals in Ansmann et al. (2019b)

To validate the performance of the newly-proposed dust datasets selection scheme, we chose 9 out of 20 AERONET sites

215   used in Ansmann et al. (2019b) to compare the obtained conversion factors. They are mainly from three typical regions, including North Africa, the Middle East, and Asia. It should be mentioned that $c_{100,\text{d}}$ values tend to be divergent when the aerosol extinction coefficient is larger than 600 Mm^{-1}. Hence, the validations were only performed for $c_{\text{v,d}}$, $c_{250,\text{d}}$, $c_{\text{s,d}}$, and

$c_{s,100,d}$. Figure 3 shows the scatters regarding the relationships between 500-nm aerosol extinction and $n_{250,d}$, v_d, s_d, and $s_{100,d}$ for pure data situations at Cape Verde, Dushanbe, and Mezaira'a. The conversion factor values are also given

220   accordingly. Here level 2.0 AOD and aerosol inversion products data were employed. PD datasets selected with the method from Shin et al. (2019) perform well as highly linear correlation can be found, with linear Pearson correlation coefficients exceeding 0.9.

Besides the three sites in figure 3, the conversion factors for the rest six sites are shown in Table 3 as well. The results for both PD and PD+DDM clusters are provided here. Generally, the regional differences in dust characteristics can be found in

225   different dust sources. $c_{v,d}$, $c_{250,d}$, and $c_{s,d}$ calculated from PD and PD+DDM datasets are almost consistent with each other, suggesting the absolute dominance of dust particles at these near/in desert sites. It should be mentioned that the large discrepancy in $c_{v,d}$ between PD and PD+DDM clusters at Dalanzadgad is attributed to the few available data points (10 for DDM and 12 for PD). Interestingly, there are larger differences in $c_{s,d}$ and $c_{s,100,d}$ between PD and PD+DDM clusters at two Middle East sites, i.e., Eilat and Mezaira'a. After a careful check, it is noted that the DDM datasets have aerosol extinction

230   coefficient values of 300-600 Mm⁻¹ and show significantly larger s_d and $s_{100,d}$ than those for PD datasets (see figure A1). The special pattern reflects the involvement of a specific type of local aerosol in the dust-dominated mixture. Moreover, the PD-DDM differences are even larger for $c_{s,100,d}$ at both sites, indicating that the additional involved aerosols may play a vital role at the particle size spectral of >100 nm. According to furthermore examination, this special pattern generally can be found at partial sites from Middle East, Africa, and polluted European cities, which, however, are rarely present at the sites

235   from East Asia, Australia, South America, and North America.

For comparison, we also plot the conversion factors in figure 4 together with those given by Ansmann et al. (2019b). $c_{v,d}$ and $c_{250,d}$ calculated from three dust datasets (DDM, DDM+PD, and A-19) coincide with each other very well. $c_{s,100,d}$ calculated from PD datasets are substantially consistent with those in Ansmann et al. (2019b), except for Dalanzadgad due to few available PD data points. $c_{s,d}$ calculated from PD datasets at two sites (CV and DK) are relatively larger than those in

240   Ansmann et al. (2019b). Using either fine mode fraction (FMF) (Lee et al., 2010) or Ångström exponent (Ansmann et al., 2019b) in the AERONRT data as dust criterion implies an assumption that dust is constrained to the coarse mode. However, the proportion between fine and coarse mode dust may alter during transport due to the quicker removal of dust particles with larger size (Yu et al., 2021); hence, the dust criterion AE <0.3 may exclude a portion of fine-mode dust (with radius <100 nm) dominated cases, resulting in an underestimation of $c_{s,d}$ at these two sites. Furthermore, region-featured emissions

245   of non-dust small particles are also possibly responsible for this discrepancy.

3.2 Dust-related conversion factors $C_{v,d}$, $C_{250,d}$, $C_{s,d}$, and $C_{s,100,d}$ at the ocean and coast sites

In this study, we chose 20 ocean and coast AERONET sites, which were classified into five region categories including the Pacific, Pacific coast (both east and west coast), Atlantic, Indian Ocean as well as Arctic Ocean (Huang et al., 2015; Zhao et al., 2022). Figure 5 shows the scatters regarding the relationships between 500-nm aerosol extinction and $n_{250,d}$, v_d,

250 s_d, and $s_{100,d}$ for both PD (in orange and red) and PD+DDM (in blue and light blue) situations at Mauna Loa (middle of Pacific), Shirahama (west coast of Pacific), Tudor Hill (west Atlantic), and Amsterdam Island (south Indian Ocean). The conversion factor values are also given accordingly. To eliminate abnormal values and retain the available dust data as much as possible, the data points with aerosol extinction of >20 Mm^{-1} participate in the calculation. PD data points generally show a good linear correlation. As for the PD+DDM cluster, three island sites show a similar good correlation except for

255 Shirahama, attributed to the small contribution of marine aerosols to total column aerosol loading (usually with a global mean AOD of ~0.05, Smirnov et al., 2009). At the Shirahama site, it is conjectured that anthropogenic aerosols considerably contribute to the column aerosol loading and lead to the spread of scatters, which reflect variations in the characteristics (size distribution, refractive index, and so on) of other aerosol components in the dust-dominated mixture.

The conversion factors $c_{v,d}$, $c_{250,d}$, $c_{s,d}$, and $c_{s,100,d}$ at the other oceanic/coast sites are also provided in Table 4. Results

260 for both PD and PD+DDM clusters are listed in case the number of PD data points is inadequate to retrieve a valid conversion factor at some sites. We also plot these dust-related conversion factors in figure 6 for comparison. According to the estimation in section 3.1, it is suggested to preferentially use the PD datasets in the calculation to avoid the potential contribution of specific local aerosols, e.g., the special pattern in $c_{s,d}$ and $c_{s,100,d}$ at Eilat and Mezaira'a (see section 3.1). Nevertheless, PD+DDM datasets may take part in the calculation, as a suboptimal option, if the sole use of PD datasets

265 cannot guarantee the validity of conversion factors (10 out of 20 sites).

As seen in figure 6, $c_{250,d}$ mainly ranges from 0.17 to 0.24 Mm cm^{-3}; the $c_{250,d}$ values calculated from PD and PD+DDM datasets agree with each other very well except for Midway Island and Nauru, indicating that few non-dust aerosols are contributing to the particle size spectral of >250 nm and $c_{250,d}$ is a relatively stable factor from region to region. For $c_{s,d}$ and $c_{s,100,d}$, their values from DDM+PD datasets mainly have a systematically positive deviation (<25%), compared with those

270 from PD datasets, which may be affected by the marine aerosols. In addition, $c_{s,d}$ and $c_{s,100,d}$ values at coast sites (especially at Shirahama, Osaka, and Hokkaido University) are considerably larger than those at remote ocean sites, revealing their higher sensitivity (compare with $c_{250,d}$) to the involvement of other aerosols. However, large differences in $c_{v,d}$ values are found not only between PD and PD+DDM datasets but also from region to region. He et al. (2019b) also reported that mixed dust in Wuhan has a smaller $c_{v,d}$ than pure dust near the source region of Asian dust. Another interesting finding for $c_{v,d}$ is

275 that the values in the Arctic are only half of those in other regions. PD data points are rarely identified in the Arctic and conversion factors are all calculated from the DDM datasets here; abundant other aerosol types in the Arctic, e.g., smoke, anthropogenic aerosol, and marine aerosol (Engelmann et al., 2021; Zhao et al., 2022), may account for the low $c_{v,d}$ values. Nevertheless, $c_{v,d}$ can be beneficial to the validation of the mass extinction efficiency, a variable combining $c_{v,d}$ and dust density, in the 3-D global dust model (Adebiyi et al., 2020; Kok et al., 2021b; Wang et al., 2021).

3.3 Dust-related conversion factors $C_{100,d}$ and χ_d at the ocean and coast sites

In addition to the INP-relevant conversion factors, the relationship between 500-nm aerosol extinction and CCN-relevant parameters $n_{100,d}$ is also studied in this section. The analysis is based on the relationship between $\log(n_{100,d})$ and $\log(\alpha_d)$ as reported by Shinozuka et al. (2015). Figure 7 shows the relationship between the aerosol extinction and particle number concentration (radius >100 nm) $n_{100,d}$ at nine oceanic/coast sites. The data points representing PD (in blue) and DDM+PD (in orange) are both plotted. Ansmann et al. (2019b) found that $\log(n_{100,d})$ and $\log(\alpha_d)$ have a good correlation when taking data points with α_d at the range of 100-600 Mm^{-1} into consideration; while, correlation strength significantly decreases and the data points trends to be dispersive once α_d values exceed 600 Mm^{-1}. The AERONET sites selected here generally show a clear atmospheric environment with limited pollution aerosols and can fulfill the constraint of $\alpha_d < 600$ Mm^{-1} except for those coast sites, e.g., Shirahama and Osaka. To retain sufficient data points, we adopted data points with α_d values ranging from 20 to 600 Mm^{-1} in our calculation.

Table 5 lists the values of $c_{100,d}$ and χ_d for both PD and DDM+PD datasets. Considering the regression coefficient >0.6 as valid analysis, attention should be paid when using the results at the coast sites Osaka, American Samoa, and Amsterdam Island. It is found that PD and DDM+PD datasets generally show a similar slope (corresponding to χ_d) in regression analysis, except for the Osaka site for which an evident intersection between two fitted lines appears, attributed to the insufficient PD data points available for fitting.

3.4 Variations in conversion factors along dust transport paths

The dust-related conversion factors may significantly vary along the way of dust transport due to the potential modifications of dust microphysical properties caused by the particle sedimentation, aging process, external mix with other aerosols, and so on. There are two main transoceanic paths of dust transport, i.e., the transatlantic one from the Saharan desert to America (Rittmeister et al, 2017; Yu et al., 2021; Dai et al., 2022) and the transpacific one from Asian dust sources (Taklimakan Desert and Gobi) to America (Guo et al., 2017; Hu et al., 2019). Here we selected several sites along these two paths to evaluate the variations of conversion factors. For the transpacific transport, six sites from Asian dust sources to America were selected, including Dushanbe, SACOL in Lanzhou, Shirahama, Midway Island, Mauna Loa, and Trinidad Head. For the Transatlantic transport, four sites from North Africa to America were selected, including Dakar, Cape Verde, ARM Graciosa, and Tudor Hill.

Figure 8 shows the conversion factors $c_{v,d}$, $c_{250,d}$, $c_{s,d}$, and $c_{s,100,d}$ at the selected sites along the two dust transport paths. It is noted that the microphysical properties of dust particles originating from the Saharan Desert and Asian dust sources are very different. Moreover, with the increase in transport distances, an evident variation tendency is observed for all the conversion factors at both transoceanic paths. $c_{v,d}$ values show a significant decline along with the transport, indicating that the proportion of dust particles in the atmospheric column tends to be smaller owing to the sedimentation. He et al. (2021b) also observed a relatively smaller $c_{v,d}$ of 0.52×10^{-12} Mm m^3 m^{-3} at the downstream area in central China compared with the

value obtained near the sources of Asian dust. $c_{250,d}$ values show a gradual increase trend along with the transport, suggesting the increased contribution of large-size sea spray aerosols in the atmospheric column. As for $c_{s,d}$, a sharp decline is observed between the values before and after transoceanic transport. The plunge of $c_{s,d}$ is more prominent for the

315 transpacific path than the transatlantic path. In contrast, $c_{s,100,d}$ values just show an inapparent enhancement. This suggests that particles with radius <100 nm should be responsible for the plunged $c_{s,d}$ after transoceanic transport.

4 Summary and conclusions

To improve the current consideration of ACIs in atmospheric circulation models, it is necessary to characterize the 3-D distribution of dust-related CCNC and INPC at a global scale. The combination of CALIOP spaceborne lidar observations

320 together with the POLIPHON method has the potential to realize this purpose. In this study, as the first step, we retrieved the essential dust-related conversion factors at the remote ocean sites where these parameters are less constrained. The historical AERONET databases were employed to calculate the conversion factors. Depolarization ratios at 1020 nm from AERONET version 3 aerosol inversion product were used to calculate the column-integrated dust ratios $R_{d,1020}$, which were further applied for identifying the dust presence within the atmospheric column (Shin et al., 2018, 2019). Compared with the use of

325 the Ångström exponent (Ansmann et al., 2019b), this treatment is beneficial for containing the fine-mode dust dominated cases (after the preferential removal of large-size dust particles during transport), mitigating the occasional interference of large-size marine aerosols, and studying the evolution of dust microphysical properties along the transoceanic transport path.

It is found that $c_{v,d}$, $c_{250,d}$, and $c_{s,100,d}$ are generally well consistent with those provided by Ansmann et al. (2019b) at nine sites near the deserts. However, $c_{s,d}$ obtained in this study are systematically larger than those given by Ansmann et al.

330 (2019b), which is attributed to the possible miss of fine-mode dust particles with radius <100 nm. For all the dust-related conversion factors, PD and PD+DDM datasets give similar results except for two Middle East sites, i.e., Eilat and Merzaira'a. Then, we calculated all the dust-related conversion factors at 20 oceanic/coast sites using both PD and PD+DDM datasets. Only 10 sites have adequate PD data points to retrieve $c_{v,d}$, $c_{250,d}$, $c_{s,d}$, and $c_{s,100,d}$. Among them, $c_{v,d}$ values are more sensitive to the influence of other aerosols involved in the atmospheric column and show large differences between PD and

335 PD+DDM clusters as well as from region to region. In addition, only 9 sites successfully obtain the CCN-relevant factors $c_{100,d}$ and χ_d in the regression analysis. Moreover, $c_{v,d}$ values are gradually decreased along with the transoceanic transport; in contrast, $c_{250,d}$ values show an increasing trend. A plunge of $c_{s,d}$ can be found after transoceanic transport, which, however, is not observed for $c_{s,100,d}$, suggesting that the discrepancy may be owing to the influence of particle size spectral of <100 nm (radius).

340 For the ocean sites, the depolarization-ratio-based method for selecting the dust-occurring data is proven to be valid and feasible. The PD data sets are suggested to be the preferential option to calculate the dust-related conversion factors. In case the available PD data points are insufficient, the PD+DDM cluster would be a suboptimal option allowing us to obtain the

conversion factors with certain accuracy and robustness. In the following work, we will conduct some case studies on dust-cloud interaction over the ocean with CALIOP spaceborne lidar observations and the dust-related conversion factors used in

345   this study. In addition, the dust-related conversion factors in polluted city sites will be examined with the same method; under this situation, the application of PD or PD+DDM data sets needs to be further discussed in depth. After that, the 3-D view of global CCNC and INPC can be anticipated to improve our current consideration of ACIs in atmospheric circulation models.

Appendix A: Additional analysis
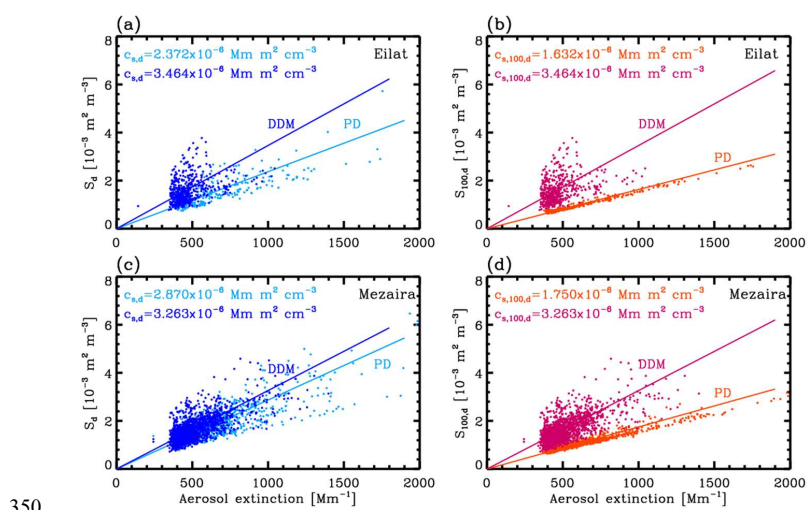
350

Figure A1: Relationship between aerosol extinction coefficient at 500 nm and surface area concentration s_d and $s_{100,d}$ (only considering particles with radius >100 nm) for pure dust (PD) and dust-dominated mixture (DDM) at two Middle East sites, i.e., (a) and (b) for Eilat, and (c) and (d) for Merzaira'a. The PD and DDM data points are determined by the AERONET V3 database (level-2.0 AOD products and level-2.0 aerosol inversions) according to the

355   **method from Shin et al. (2019). The corresponding dust-related conversion factors $c_{s,d}$ and $c_{s,100,d}$ are also given, respectively.**

Data availability

All data used in this work can be accessed through the AERONET home page at https://aeronet.gsfc.nasa.gov/ (AERONET, 2022).

Author Contributions

Yun He conceived the research, analyzed the data, acquired the research funding, and wrote the manuscript. Zhenping Yin conceived the research, participated in scientific discussions, and reviewed and proofread the manuscript. Albert Ansmann reviewed the manuscript and participated in scientific discussions. Fuchao Liu and Longlong Wang reviewed and proofread the manuscript. Dongzhe Jing and Huijia Shen participated in the data processing.

Competing interests

The authors declare that they have no conflict of interest.

Acknowledgments

The authors thank all PIs of the AERONET sites used in this study for maintaining their instruments and providing their data to the community.

Financial support

This research has been supported by the National Natural Science Foundation of China (grant nos. 42005101, 41927804, and 42205130), the Fundamental Research Funds for the Central Universities (grant no. 2042021kf1066), and the Meridian Space Weather Monitoring Project (China).

References

AERONET: AERONET aerosol data base, available at: http://aeronet.gsfc.nasa.gov/, last access: 15 December 2022.

Adebiyi, A. A., Kok, J. F., Wang, Y., Ito, A., Ridley, D. A., Nabat, P., and Zhao, C.: Dust Constraints from joint Observational-modelling-experimental analysis (DustCOMM): comparison with measurements and model simulations, Atmos. Chem. Phys., 20, 829–863, https://doi.org/10.5194/acp-20-829-2020, 2020.

Albrecht, B. A.: Aerosols, cloud microphysics, and fractional cloudiness, Science, 245, 1227–1230, https://doi.org/10.1126/science.245.4923.1227, 1989.

Ansmann, A., Seifert, P., Tesche, M., and Wandinger, U.: Profiling of fine and coarse particle mass: case studies of Saharan dust and Eyjafjallajökull/Grimsvötn volcanic plumes, Atmos. Chem. Phys., 12, 9399–9415, https://doi.org/10.5194/acp-12-9399-2012, 2012.

Ansmann, A., Mamouri, R.-E., Bühl, J., Seifert, P., Engelmann, R., Hofer, J., Nisantzi, A., Atkinson, J. D., Kanji, Z. A., Sierau, B., Vrekoussis, M., and Sciare, J.: Ice-nucleating particle versus ice crystal number concentration in

altocumulus and cirrus embedded in Saharan dust: A closure study, Atmos. Chem. Phys., 19, 15087–15115, https://doi.org/10.5194/acp-19-15087-2019, 2019a.

Ansmann, A., Mamouri, R.-E., Hofer, J., Baars, H., Althausen, D., and Abdullaev, S. F.: Dust mass, cloud condensation nuclei, and ice-nucleating particle profiling with polarization lidar: updated POLIPHON conversion factors from global AERONET analysis, Atmos. Meas. Tech., 12, 4849–4865, https://doi.org/10.5194/amt-12-4849-2019, 2019b.

Ansmann, A., Ohneiser, K., Mamouri, R.-E., Knopf, D. A., Veselovskii, I., Baars, H., Engelmann, R., Foth, A., Jimenez, C., Seifert, P., and Barja, B.: Tropospheric and stratospheric wildfire smoke profiling with lidar: mass, surface area, CCN, and INP retrieval, Atmos. Chem. Phys., 21, 9779–9807, https://doi.org/10.5194/acp-21-9779-2021, 2021.

Choudhury, G. and Tesche, M.: Estimating cloud condensation nuclei concentrations from CALIPSO lidar measurements, Atmos. Meas. Tech., 15, 639–654, https://doi.org/10.5194/amt-15-639-2022, 2022.

Cziczo, D., Froyd, K., Hoose, C., Jensen, E., Diao, M., Zondlo, M., Smith, J., Twohy, C., and Murphy, D.: Clarifying the dominant sources and mechanisms of cirrus cloud formation, Science, 340, 1320–1324, https://doi.org/10.1126/science.1234145, 2013.

Dubovik, O. and King, M.: A flexible inversion algorithm for retrieval of aerosol optical properties from sun and sky radiance measurements, J. Geophys. Res., 105, 20673–20696, https://doi.org/10.1029/2000JD900282, 2000.

Dubovik, O., Smirnov, A., Holben, B., King, M., Kaufman, Y., Eck, T., and Slutsker, I.: Accuracy assessments of aerosol optical properties retrieved from Aerosol Robotic Network (AERONET) sun and sky radiance measurements, J. Geophys. Res., 105, 9791–9806, https://doi.org/10.1029/2000JD900040, 2000.

Dubovik, O., Sinyuk, A., Lapyonok, T., Holben, B. N., Mishchenko, M., Yang, P., Eck, T. F., Volten, H., Muñoz, O., and Veihelmann, B.: Application of spheroid models to account for aerosol particle nonsphericity in remote sensing of desert dust, J. Geophys. Res., 111, D11208, https://doi.org/10.1029/2005JD006619, 2006.

Dai, G., Sun, K., Wang, X., Wu, S., E, X., Liu, Q., and Liu, B.: Dust transport and advection measurement with spaceborne lidars ALADIN and CALIOP and model reanalysis data, Atmos. Chem. Phys., 22, 7975–7993, https://doi.org/10.5194/acp-22-7975-2022, 2022.

DeMott, P., Prenni, A., Liu, X., Kreidenweis, S., Petters, M., Twohy, C., Richardson, M., Eidhammer, T., and Rogers, D.: Predicting global atmospheric ice nuclei distributions and their impacts on climate, P. Natl. Acad. Sci. USA, 107, 11217–11222. https://doi.org/10.1073/pnas.0910818107, 2010.

DeMott, P., Prenni, A., McMeeking, G., Sullivan, R., Petters, M., Tobo, Y., Niemand, M., Möhler, O., Snider, J., Wang, Z., and Kreidenweis, S.: Integrating laboratory and field data to quantify the immersion freezing ice nucleation activity of mineral dust particles, Atmos. Chem. Phys., 15, 393–409, https://doi.org/10.5194/acp-15-393-2015, 2015.

Engelmann, R., Ansmann, A., Ohneiser, K., Griesche, H., Radenz, M., Hofer, J., Althausen, D., Dahlke, S., Maturilli, M., Veselovskii, I., Jimenez, C., Wiesen, R., Baars, H., Bühl, J., Gebauer, H., Haarig, M., Seifert, P., Wandinger, U., and Macke, A.: Wildfire smoke, Arctic haze, and aerosol effects on mixed-phase and cirrus clouds over the North Pole

region during MOSAiC: an introduction, Atmos. Chem. Phys., 21, 13397–13423, https://doi.org/10.5194/acp-21-13397-2021, 2021.

Fernald, F. G.: Analysis of atmospheric lidar observations: some comments, Appl. Optics, 23, 652–653, https://doi.org/10.1364/AO.23.000652, 1984.

Froyd, K. D., Yu, P., Schill, G. P. Brock, C. A., Kupc, A., Williamson, C. J., Jensen, E. J., Ray, E., Rosenlof, K. H., Bian, H., Darmenov, A. S., Colarco, P. R., Diskin, G. S., Bui, T., and Murphy, D. M.: Dominant role of mineral dust in cirrus cloud formation revealed by global-scale measurements, Nat. Geosci. 15, 177–183, https://doi.org/10.1038/s41561-022-00901-w, 2022.

Giles, D., Sinyuk, A., Sorokin, M., Schafer, J., Smirnov, A., Slutsker, I., Eck, T., Holben, B., Lewis, J., Campbell, J., Welton, E., Korkin, S., and Lyapustin, A.: Advancements in the Aerosol Robotic Network (AERONET) Version 3 database – automated near-real-time quality control algorithm with improved cloud screening for Sun photometer aerosol optical depth (AOD) measurements, Atmos. Meas. Tech., 12, 169-209, https://doi.org/10.5194/amt-12-169-2019, 2019.

Guo, J., Lou, M., Miao, Y., Wang, Y., Zeng, Z., Liu, H., He, J., Xu, H., Wang, F., Min, M., and Zhai, P.: Trans-Pacific transport of dust aerosol originated from East Asia: Insights gained from multiple observations and modeling, Environ. Pollut., 230, 1030–1039, https://doi.org/10.1016/j.envpol.2017.07.062, 2017.

Haarig, M., Ansmann, A., Gasteiger, J., Kandler, K., Althausen, D., Baars, H., Radenz, M., and Farrell, D. A.: Dry versus wet marine particle optical properties: RH dependence of depolarization ratio, backscatter, and extinction from multiwavelength lidar measurements during SALTRACE, Atmos. Chem. Phys., 17, 14199, https://doi.org/10.5194/acp-2017-545, 2017.

Haarig, M., Walser, A., Ansmann, A., Dollner, M., Althausen, D., Sauer, D., Farrell, D., and Weinzierl, B.: Profiles of cloud condensation nuclei, dust mass concentration, and ice-nucleating-particle-relevant aerosol properties in the Saharan Air Layer over Barbados from polarization lidar and airborne in situ measurements, Atmos. Chem. Phys., 19, 13773–13788, https://doi.org/10.5194/acp-19-13773-2019, 2019.

Haarig, M., Ansmann, A., Engelmann, R., Baars, H., Toledano, C., Torres, B., Althausen, D., Radenz, M., and Wandinger, U.: First triple-wavelength lidar observations of depolarization and extinction-to-backscatter ratios of Saharan dust, Atmos. Chem. Phys., 22, 355–369, https://doi.org/10.5194/acp-22-355-2022, 2022.

He, Y. and Yi, F.: Dust aerosols detected using a ground-based polarization lidar and CALIPSO over Wuhan (30.5N, 114.4E), China, Adv. Meteorol., 2015, 536762, https://doi.org/10.1155/2015/536762, 2015.

He, Y., Yi, F., Yi, Y., Liu, F., and Zhang, Y.: Heterogeneous nucleation of midlevel cloud layer influenced by transported Asian dust over Wuhan (30.5N, 114.4E), China, J. Geophys. Res.-Atmos., 126, e2020JD033394, https://doi.org/10.1029/2020JD033394, 2021a.

He, Y., Zhang, Y., Liu, F., Yin, Z., Yi, Y., Zhan, Y., and Yi, F.: Retrievals of dust-related particle mass and ice-nucleating particle concentration profiles with ground-based polarization lidar and sun photometer over a megacity in central China, Atmos. Meas. Tech., 14, 5939–5954, https://doi.org/10.5194/amt-14-5939-2021, 2021b.

He, Y., Yin, Z., Liu, F., and Yi, F.: Technical note: Identification of two ice-nucleating regimes for dust-related cirrus clouds based on the relationship between number concentrations of ice-nucleating particles and ice crystals, Atmos. Chem. Phys., 22, 13067–13085, https://doi.org/10.5194/acp-22-13067-2022, 2022a.

He, Y., Yi, F., Liu, F., Yin, Z., and Zhou, J.: Ice nucleation of cirrus clouds related to the transported dust layer observed by ground-based lidars over Wuhan, China, Adv. Atmos. Sci., 39(12), 2071-2086, https://doi.org/10.1007/s00376-021-1192-x, 2022b.

He, Y., Yi, F., Yin, Z., Liu, F., Yi, Y., and Zhou, J.: Mega Asian dust event over China on 27–31 March 2021 observed with space-borne instruments and ground-based polarization lidar, Atmos. Environ., 285, 119238, https://doi.org/10.1016/j.atmosenv.2022.119238, 2022c.

Hofer, J., Ansmann, A., Althausen, D., Engelmann, R., Baars, H., Abdullaev, S. F., and Makhmudov, A. N.: Long-term profiling of aerosol light extinction, particle mass, cloud condensation nuclei, and ice-nucleating particle concentration over Dushanbe, Tajikistan, in Central Asia, Atmos. Chem. Phys., 20, 4695–4711, https://doi.org/10.5194/acp-20-4695-2020, 2020.

Holben, B., Eck, T., Slutsker, I., Tanré, D., Buis, J., Setzer, A., Vermote, E., Reagan, J., Kaufman, Y., Nakajima, T., Lavenu, F., Jankowiak, I., and Smirnov, A.: AERONET – A federated instrument network and data archive for aerosol characterization, Remote Sens. Environ., 66, 1–16, https://doi.org/10.1016/s0034-4257(98)00031-5, 1998.

Hu, Q., Wang, H., Goloub, P., Li, Z., Veselovskii, I., Podvin, T., Li, K., and Korenskiy, M.: The characterization of Taklamakan dust properties using a multiwavelength Raman polarization lidar in Kashi, China, Atmos. Chem. Phys., 20, 13817–13834, https://doi.org/10.5194/acp-20-13817-2020, 2020.

Hu, Z., Huang, J., Zhao, C., Ma, Y., Jin, Q., Qian, Y., Leung, L. R., Bi, J., and Ma, J.: Trans-Pacific transport and evolution of aerosols: spatiotemporal characteristics and source contributions, Atmos. Chem. Phys., 19, 12709–12730, https://doi.org/10.5194/acp-19-12709-2019, 2019.

Huang, Z., Huang, J., Hayasaka, T., Wang, S., Zhou, T., and Jin, H.: Short-cut transport path for Asian dust directly to the Arctic: a case study, Environ. Res. Lett., 10, 114018, https://doi.org/10.1088/1748-9326/10/11/114018, 2015.

Illingworth, A. J., Barker, H. W., Beljaars, A., Ceccaldi, M., Chepfer, H., Clerbaux, N., Cole, J., Delanoë, J., Domenech, C., Donovan, D. P., Fukuda, S., Hirakata, M., Hogan, R. J., Huenerbein, A., Kollias, P., Kubota, T., Nakajima, T., Nakajima, T. Y., Nishizawa, T., Ohno, Y., Okamoto, H., Oki, R., Sato, K., Satoh, M., Shephard, M., Velázquez-Blázquez, A., Wandinger, U., Wehr, T., van Zadelhoff, G.-J.: The EarthCARE Satellite: The next step forward in global measurements of clouds, aerosols, precipitation and radiation, B. Am. Meteorol. Soc., 96, 1311–1332, doi.org/10.1175/BAMS-D-12-00227.1, 2015.

IPCC: Climate Change 2013: The Physical Science Basis, Contribution of Working Group I to the Fifth Assessment Report of the Intergovernmental Panel on Climate Change, Cambridge University Press, Cambridge, United Kingdom and New York, USA, https://doi.org/10.1017/CBO9781107415324, 2013.

Kanji, Z. A., Ladino, L. A., Wex, H., Boose, Y., Burkert-Kohn, M., Cziczo, D. J., and Krämer, M.: Overview of ice nucleating particles, Meteor. Mon., 58, 1.1–1.33, https://doi.org/10.1175/AMSMONOGRAPHS-D-16-0006.1, 2017.

Kok, J. F., Adebiyi, A. A., Albani, S., Balkanski, Y., Checa-Garcia, R., Chin, M., Colarco, P. R., Hamilton, D. S., Huang, Y.,
Ito, A., Klose, M., Li, L., Mahowald, N. M., Miller, R. L., Obiso, V., Pérez García-Pando, C., Rocha-Lima, A., and
490 Wan, J. S.: Contribution of the world's main dust source regions to the global cycle of desert dust, Atmos. Chem. Phys.,
21, 8169–8193, https://doi.org/10.5194/acp-21-8169-2021, 2021a.

Kok, J. F., Adebiyi, A. A., Albani, S., Balkanski, Y., Checa-Garcia, R., Chin, M., Colarco, P. R., Hamilton, D. S., Huang, Y.,
Ito, A., Klose, M., Leung, D. M., Li, L., Mahowald, N. M., Miller, R. L., Obiso, V., Pérez García-Pando, C., Rocha-
Lima, A., Wan, J. S., and Whicker, C. A.: Improved representation of the global dust cycle using observational
495 constraints on dust properties and abundance, Atmos. Chem. Phys., 21, 8127–8167, https://doi.org/10.5194/acp-21-
8127-2021, 2021b.

Lee, J., Kim, J., Song, C., Kim, S., Chun, Y., Sohn, B., and Holben, B.: Characteristics of aerosol types from AERONET
sun-photometer measurements, Atmos. Environ., 44, 3110–3117, https://doi.org/10.1016/j.atmosenv.2010.05.035, 2010.

Lenhardt, E. D., Gao, L., Redemann, J., Xu, F., Burton, S. P., Cairns, B., Chang, I., Ferrare, R. A., Hostetler, C. A., Saide, P.
500 E., Howes, C., Shinozuka, Y., Stamnes, S., Kacarab, M., Dobracki, A., Wong, J., Freitag, S., and Nenes, A.: Use of
Lidar Aerosol Extinction and Backscatter Coefficients to Estimate Cloud Condensation Nuclei (CCN) Concentrations
in the Southeast Atlantic, Atmos. Meas. Tech. Discuss. [preprint], https://doi.org/10.5194/amt-2022-262, in review,
2022.

Li, G., Wieder, J., Pasquier, J. T., Henneberger, J., and Kanji, Z. A.: Predicting atmospheric background number
505 concentration of ice-nucleating particles in the Arctic, Atmos. Chem. Phys., 22, 14441–14454,
https://doi.org/10.5194/acp-22-14441-2022, 2022.

Liu, C., Yin, Z., He, Y., and Wang, L.: Climatology of dust aerosols over the Jianghan Plain revealed with space-borne
instruments and MERRA-2 reanalysis data during 2006–2021. Remote Sens., 14(17), 4414.
https://doi.org/10.3390/rs14174414, 2022.

510 Mamouri, R. E., Ansmann, A., Nisantzi, A., Kokkalis, P., Schwarz, A., and Hadjimitsis, D.: Low Arabian extinction-to-
backscatter ratio, Geophys. Res. Lett., 40, 4762–4766. https://doi.org/10.1002/grl.50898, 2013.

Mamouri, R. E. and Ansmann, A.: Fine and Coarse dust separation with polarization lidar, Atmos. Meas. Tech., 7, 3717–
3735. https://doi.org/10.5194/amt-7-3717-2014, 2014.

Mamouri, R. E. and Ansmann, A.: Estimated desert-dust ice nuclei profiles from polarization lidar: methodology and case
515 studies, Atmos. Chem. Phys., 15, 3463–3477, https://doi.org/10.5194/acp-15-3463-2015, 2015.

Mamouri, R. E. and Ansmann, A.: Potential of polarization lidar to provide profiles of CCN- and INP-relevant aerosol
parameters, Atmos. Chem. Phys., 16, 5905–5931, https://doi.org/10.5194/acp-16-5905-2016, 2016.

Mamouri, R. E. and Ansmann, A.: Potential of polarization/Raman lidar to separate fine dust, coarse dust, maritime, and
anthropogenic aerosol profiles, Atmos. Meas. Tech., 10, 3403–3427, https://doi.org/10.5194/amt-10-3403-2017, 2017.

520   Marinou, E., Tesche, M., Nenes, A., Ansmann, A., Schrod, J., Mamali, D., Tsekeri, A., Pikridas, M., Baars, H., Engelmann,
       R., Voudouri, K.-A., Solomos, S., Sciare, J., Groß, S., Ewald, F., and Amiridis, V.: Retrieval of ice-nucleating particle
       concentrations from lidar observations and comparison with UAV in situ measurements, Atmos. Chem. Phys., 19,
       11315–11342, https://doi.org/10.5194/acp-19-11315-2019, 2019.

       Moore, R. H., Cerully, K., Bahreini, R., Brock, C. A., Middlebrook, A. M., and Nenes, A.: Hygroscopicity and composition
525   of California CCN during summer 2010, J. Geophys. Res.-Atmos., 117, D00V12,
       https://doi.org/10.1029/2011JD017352, 2012.

       Müller, D., Ansmann, A., Mattis, I., Tesche, M., Wandinger, U., Althausen, D., and Pisani, G.: Aerosol-type-dependent lidar
       ratios observed with Raman lidar, J. Geophys. Res., 112, D16202, https://doi.org/10.1029/2006JD008292, 2007.

       Murray, B. J., O'Sullivan, D., Atkinson, J. D., and Webb, M. E.: Ice nucleation by particles immersed in supercooled cloud
530   droplet, Chem. Soc. Rev., 41, 6519–6554, https://doi.org/10.1039/c2cs35200a, 2012.

       Niemand, M., Möhler, O., Vogel, B., Vogel, H., Hoose, C., Connolly, P., Klein, H., Bingemer, H., DeMott, P., Skrotzki, J.,
       and Leisner, T.: Parameterisation of immersion freezing on mineral dust particles: an application in a regional scale
       model, J. Atmos. Sci., 69, 3077–3092, https://doi.org/10.1175/JAS-D-11-0249.1, 2012.

       Noh, Y., Müller, D., Lee, K., Kim, K., Lee, K., Shimizu, A., Sano, I., and Park, C. B.: Depolarization ratios retrieved by
535   AERONET sun–sky radiometer data and comparison to depolarization ratios measured with lidar, Atmos. Chem. Phys.,
       17, 6271–6290, https://doi.org/10.5194/acp-17-6271-2017, 2017.

       Patel, P., Jiang, J., Gautam, R., Gadhavi, H., Kalashnikova, O., Garay, M., Gao, L., Xu, F., and Omar, A.: Resolving Vertical
       Profile of Cloud Condensation Nuclei Concentrations from Spaceborne Lidar Measurements, Atmos. Chem. Phys.
       Discuss. [preprint], https://doi.org/10.5194/acp-2022-547, in review, 2022.

540   Peng, L., Yi, F., Liu, F., Yin, Z. and He, Y.: Optical properties of aerosol and cloud particles measured by a single-line-
       extracted pure rotational Raman lidar, Opt. Express, 29(14), 21947-21964. https://doi.org/10.1364/OE.427864, 2021.

       Philip, S., Martin, R. V., Snider, G., Weagle, C. L., van Donkelaar, A., Brauer, M., Henze, D. K., Klimont, Z.,
       Venkataraman, C., Guttikunda, S. K., and Zhang, Q.: Anthropogenic fugitive, combustion and industrial dust is a
       significant, underrepresented fine particulate matter source in global atmospheric models, Environ. Res. Lett., 12,
545   044018, https://doi.org/10.1088/1748-9326/aa65a4, 2017.

       Rittmeister, F., Ansmann, A., Engelmann, R., Skupin, A., Baars, H., Kanitz, T., and Kinne, S.: Profiling of Saharan dust
       from the Caribbean to western Africa – Part 1: Layering structures and optical properties from shipborne
       polarization/Raman lidar observations, Atmos. Chem. Phys., 17, 12963–12983, https://doi.org/10.5194/acp-17-12963-
       2017, 2017.

550   Rosenfeld, D., Andreae, M. O., Asmi, A., Chin, M., Leeuw, G., Donovan, D. P., Kahn, R., Kinne, S., Kivekäs, N., Kulmala,
       M., Lau, W., Schmidt, K. S., Suni, T., Wagner, T., Wild, M., and Quaas, J.: Global observations of aerosol-cloud-
       precipitation-climate interactions, Rev. Geophys., 52, 750–808, https://doi.org/10.1002/2013RG000441, 2014.

Shin, S.-K., Tesche, M., Kim, K., Kezoudi, M., Tatarov, B., Müller, D., and Noh, Y.: On the spectral depolarisation and lidar ratio of mineral dust provided in the AERONET version 3 inversion product, Atmos. Chem. Phys., 18, 12735–12746, https://doi.org/10.5194/acp-18-12735-2018, 2018.

555 Shin, S.-K., Tesche, M., Noh, Y., and Müller, D.: Aerosol-type classification based on AERONET version 3 inversion products, Atmos. Meas. Tech., 12, 3789–3803, https://doi.org/10.5194/amt-12-3789-2019, 2019.

Shinozuka, Y., Clarke, A. D., Nenes, A., Jefferson, A., Wood, R., McNaughton, C. S., Ström, J., Tunved, P., Redemann, J., Thornhill, K. L., Moore, R. H., Lathem, T. L., Lin, J. J., and Yoon, Y. J.: The relationship between cloud condensation

560 nuclei (CCN) concentration and light extinction of dried particles: indications of underlying aerosol processes and implications for satellitebased CCN estimates, Atmos. Chem. Phys., 15, 7585–7604, https://doi.org/10.5194/acp-15-7585-2015, 2015.

Sinyuk, A., Holben, B. N., Eck, T. F., Giles, D. M., Slutsker, I., Korkin, S., Schafer, J. S., Smirnov, A., Sorokin, M., and Lyapustin, A.: The AERONET Version 3 aerosol retrieval algorithm, associated uncertainties and comparisons to

565 Version 2, Atmos. Meas. Tech., 13, 3375–3411, https://doi.org/10.5194/amt-13-3375-2020, 2020.

Smirnov, A., Holben, B. N., Slutsker, I., Giles, D. M., McClain, C. R., Eck, T. F., S. Sakerin, M., Macke, A., Croot, P., Zibordi, G., Quinn, P. K., Sciare, J., Kinne, S., Harvey, M., Smyth, T. J., Piketh, S., Zielinski, T., Proshutinsky, A., Goes, J. I., Nelson, N. B., Larouche, P., Radionov, V. F., Goloub, P., Krishna Moorthy, K., Matarrese, R., Robertson, E. J., and Jourdin, F.: Maritime Aerosol Network as a component of Aerosol Robotic Network, J. Geophys. Res., 114,

570 D06204, doi:10.1029/2008JD011257, 2009.

Smirnov, A., Holben, B. N., Giles, D. M., Slutsker, I., O'Neill, N. T., Eck, T. F., Macke, A., Croot, P., Courcoux, Y., Sakerin, S. M., Smyth, T. J., Zielinski, T., Zibordi, G., Goes, J. I., Harvey, M. J., Quinn, P. K., Nelson, N. B., Radionov, V. F., Duarte, C. M., Losno, R., Sciare, J., Voss, K. J., Kinne, S., Nalli, N. R., Joseph, E., Moorthy, K. K., Covert, D. S., Gulev, S. K., Milinevsky, G., Larouche, P., Belanger, S., Horne, E., Chin, M., Remer, L. A., Kahn, R. A., Reid, J. S.,

575 Schulz, M., Heald, C. L., Zhang, J., Lapina, K., Kleidman, R. G., Griesfeller, J., Gaitley, B. J., Tan, Q., and Diehl, T. L.: Maritime aerosol network as a component of AERONET - first results and comparison with global aerosol models and satellite retrievals, Atmos. Meas. Tech., 4, 583-597, https://doi.org/10.5194/amt-4-583-2011, 2011.

Spänkuch, D., Hellmuth, O., and Görsdorf, U.: What is a cloud? Toward a more precise definition, B. Am. Meteorol. Soc., 103(8), E1894-E1929, https://doi.org/10.1175/BAMS-D-21-0032.1.

580 Steinke, I., Hoose, C., Möhler, O., Connolly, P., and Leisner, T.: A new temperature- and humidity-dependent surface site density approach for deposition ice nucleation, Atmos. Chem. Phys., 15, 3703–3717, https://doi.org/10.5194/acp-15-3703-2015, 2015.

Stier, P.: Limitations of passive remote sensing to constrain global cloud condensation nuclei, Atmos. Chem. Phys., 16, 6595–6607, https://doi.org/10.5194/acp-16-6595-2016, 2016.

585 Toledano, C., Torres, B., Velasco-Merino, C., Althausen, D., Groß, S., Wiegner, M., Weinzierl, B., Gasteiger, J., Ansmann, A., González, R., Mateos, D., Farrel, D., Müller, T., Haarig, M., and Cachorro, V. E.: Sun photometer retrievals of

Saharan dust properties over Barbados during SALTRACE, Atmos. Chem. Phys., 19, 14571–14583, https://doi.org/10.5194/acp-19-14571-2019, 2019.

Twomey, S.: Pollution and the planetary albedo, Atmos. Environ., 8, 1251–1256, https://doi.org/10.1016/0004-6981(74)90004-3, 1974.

Tesche, M., Ansmann, A., Müller, D., Althausen, D., Engelmann, R., Freudenthaler, V., and Groß, S.: Vertically resolved separation of dust and smoke over Cape Verde using multiwavelength Raman and polarization lidars during Saharan Mineral Dust Experiment 2008, J. Geophys. Res., 114, D13202, https://doi.org/10.1029/2009JD011862, 2009.

Ullrich, R., Hoose, C., Möhler, O., Niemand, M., Wagner, R., Höhler, K., Hiranuma, N., Saathoff, H., and Leisner, T.: A new ice nucleation active site parameterization for desert dust and soot, J. Atmos. Sci., 74, 699–717, https://doi.org/10.1175/JASD-16-0074.1, 2017.

Wang, J., Cubison, M. J., Aiken, A. C., Jimenez, J. L., and Collins, D. R.: The importance of aerosol mixing state and size-resolved composition on CCN concentration and the variation of the importance with atmospheric aging of aerosols, Atmos. Chem. Phys., 10, 7267–7283, https://doi.org/10.5194/acp-10-7267-2010, 2010.

Wang, T.; Han, Y., Hua, W., Tang, J., Huang, J., Zhou, T., Huang, Z., Bi, J., and Xie, H.: Profiling dust mass concentration in Northwest China using a joint lidar and sun-photometer setting, Remote Sens., 13, 1099, https://doi.org/10.3390/rs13061099, 2021.

Wieder, J., Ihn, N., Mignani, C., Haarig, M., Bühl, J., Seifert, P., Engelmann, R., Ramelli, F., Kanji, Z. A., Lohmann, U., and Henneberger, J.: Retrieving ice-nucleating particle concentration and ice multiplication factors using active remote sensing validated by in situ observations, Atmos. Chem. Phys., 22, 9767–9797, https://doi.org/10.5194/acp-22-9767-2022, 2022.

Winker, D., Hunt, W., and McGill, M.: Initial performance assessment of CALIOP, Geophys. Res. Lett., 34, L19803, https://doi.org/10.1029/2007GL030135, 2007.

Yin, Z., Ansmann, A., Baars, H., Seifert, P., Engelmann, R., Radenz, M., Jimenez, C., Herzog, A., Ohneiser, K., and Hanbuch, K.: Aerosol measurements with a shipborne Sun–sky–lunar photometer and collocated multiwavelength Raman polarization lidar over the Atlantic Ocean, Atmos. Meas. Tech., 12, 5685-5698, https://doi.org/10.5194/amt-12-5685-2019, 2019.

Yin, Z., Yi, F., He, Y., Liu, D., Yu, C., and Zhang, Y.: Asian dust impacts on heterogeneous ice formation at Wuhan based on polarization lidar measurements, Atmos. Environ., 246, 118166, https://doi.org/10.1016/j.atmosenv.2020.118166, 2021.

Yu, H., Tan, Q., Zhou, L., Zhou, Y., Bian, H., Chin, M., Ryder, C. L., Levy, R. C., Pradhan, Y., Shi, Y., Song, Q., Zhang, Z., Colarco, P. R., Kim, D., Remer, L. A., Yuan, T., Mayol-Bracero, O., and Holben, B. N.: Observation and modeling of the historic "Godzilla" African dust intrusion into the Caribbean Basin and the southern US in June 2020, Atmos. Chem. Phys., 21, 12359–12383, https://doi.org/10.5194/acp-21-12359-2021, 2021.

620   Zhang, C., Wu, Z., Chen, J., Chen, J., Tang, L., Zhu, W., Pei, X., Chen, S., Tian, P., Guo, S., Zeng, L., Hu, M., and Kanji, Z. A.: Ice-nucleating particles from multiple aerosol sources in the urban environment of Beijing under mixed-phase cloud conditions, Atmos. Chem. Phys., 22, 7539–7556, https://doi.org/10.5194/acp-22-7539-2022, 2022.

Zhao, X., Huang, K., Fu, J. S., and Abdullaev, S. F.: Long-range transport of Asian dust to the Arctic: identification of transport pathways, evolution of aerosol optical properties, and impact assessment on surface albedo changes, Atmos.
625   Chem. Phys., 22, 10389–10407, https://doi.org/10.5194/acp-22-10389-2022, 2022.

Table 1. Dust-related parameters of optical properties, cloud condensation nuclei, and ice-nucleating particles calculated by the POLIPHON method (Tesche et al., 2009; Marinou et al., 2019; Ansmann et al., 2019b). D10, D15, U17, N12, and S15 refer to the respective INP parameterization in DeMott et al. (2010), DeMott et al. (2015), Ullrich et al. (2017), Niemand et al. (2012), and Steinke et al. (2015). The subscript 'ss' denotes water supersaturation.

Dust-related parameters	Computation	Uncertainty	References
Dust backscatter β_d (Mm^{-1} sr^{-1})	$\beta_\mathrm{d}(z) = \beta_\mathrm{p}(z) \dfrac{(\delta_\mathrm{p}(z) - \delta_\mathrm{nd})(1 + \delta_\mathrm{d})}{(\delta_\mathrm{d} - \delta_\mathrm{nd})\left(1 + \delta_\mathrm{p}(z)\right)}$ $\delta_\mathrm{d} = 0.31,\ \delta_\mathrm{nd} = 0.05$	10-30%	(Tesche et al., 2009)
Dust extinction α_d (Mm^{-1})	$\alpha_\mathrm{d}(z) = LR_\mathrm{d} \times \beta_\mathrm{d}(z)$	15-25%	(Ansmann et al., 2019b)
Dust mass conc. M_d (µg m^{-3})	$M_\mathrm{d}(z) = \rho_\mathrm{d} \times \alpha_\mathrm{d}(z) \times c_\mathrm{v,d}$ $\rho_\mathrm{d} = 2.6$ g cm^{-3}	20-30%	(Ansmann et al., 2019b)
Particle number conc. (r> 250 nm) $n_{250,\mathrm{d}}$ (cm^{-3})	$n_{250,\mathrm{d}}(z) = \alpha_\mathrm{d}(z) \times c_{250,\mathrm{d}}$	25-35%	(Ansmann et al., 2019b)
Particle surface conc. S_d (m² cm^{-3})	$S_\mathrm{d}(z) = \alpha_\mathrm{d}(z) \times c_\mathrm{s,d}$	30-40%	(Ansmann et al., 2019b)
Particle surface conc. (r> 100 nm) $S_{100,\mathrm{d}}$ (m² cm^{-3})	$S_{100,\mathrm{d}}(z) = \alpha_\mathrm{d}(z) \times c_\mathrm{s,100,d}$	20-30%	(Ansmann et al., 2019b)
$n_\mathrm{INP,d}$ (L^{-1}) from $n_{250,\mathrm{d}}$	INP parameterization D10 and D15	50-500%	(DeMott et al., 2010, 2015)
$n_\mathrm{INP,d}$ (L^{-1}) from S_d and $S_{100,\mathrm{d}}$	INP parameterization U17, N12 and S15	50-500%	(Niemand et al., 2012; Steinke et al. 2015; Ullrich et al., 2017)
$n_\mathrm{CCN,ss,d}$ (L^{-1}) from $n_{100,\mathrm{d}}$	$n_\mathrm{CCN,ss,d}(z) = f_\mathrm{ss,d} \times n_{100,\mathrm{d}}(z)$	50-200%	(Mamouri and Ansmann, 2016)
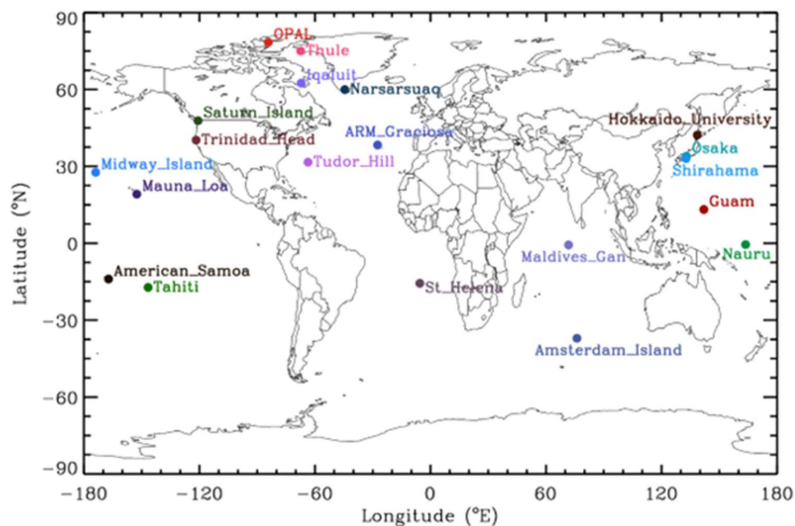
Figure 1: Overview of the ocean and coast AERONET sites used in this study. Labels for each site are taken from AERONET site list.

Table 2. Basic information of the AERONET sites selected for dust-related POLIPHON conversion factors calculation near the deserts (from North Africa, the Middle East, and Asia) and over the ocean and coast (from the Pacific, Pacific coast, Atlantic, Indian Ocean, and Arctic Ocean) regions, including the site name and abbreviation, period, and location. The available number of data points for total, dust-dominated mixture (DDM), and pure dust (PD) in AERONET version 3 aerosol inversion products (level 2.0 for near-desert cluster and level 1.5 for oceanic/coast cluster) are also given, respectively.

640

	Site (Abbreviation)	Period	Location	Total Obs.	DDM Obs.	PD Obs.
Pacific	Tahiti (TA)	1999-2010	41.05N, 124.15W	1210	247	6
	Nauru (NR)	1999-2013	0.52S, 166.92E	1379	141	12
	Midway_Island (MI)	2001-2015	28.21N, 177.38W	1663	351	26
	American_Samoa (AS)	2014-2022	14.25S, 170.56W	1080	197	14
	Guam (GA)	2006-2009	13.43N, 144.80E	239	33	2
	Mauna_Loa (ML)	1994-2022	19.54N, 155.58W	30384	1481	27
Pacific Coast	Hokkaido_University (HU)	2015-2022	43.08N, 141.34E	3524	321	11
	Osaka (OS)	2000-2022	34.65N, 135.59E	3296	99	13
	Shirahama (SH)	2000-2022	33.69N, 135.36E	9095	1421	68
	Saturn_Island (SI)	1997-2022	48.78N, 123.13W	5986	527	0
	Trinidad_Head (TR)	2005-2017	41.05N, 124.15W	3978	678	18
Atlantic	ARM_Graciosa (AG)	2013-2022	39.09N, 28.03W	2549	218	50
	Tudor_Hill (TH)	2007-2022	32.26N, 64.88W	2222	502	40
	St_Helena (SH)	2016-2022	15.94S, 5.67W	294	18	0
Indian Ocean	Maldives_Gan (MG)	2018-2022	0.69S, 73.15E	1153	190	4
	Amsterdam_Island (AI)	2002-2022	37.80S, 77.57E	1241	216	25
Arctic Ocean	Narsarsuaq (NA)	2013-2022	61.16N, 45.42W	2918	139	2
	Thule (TL)	2007-2022	76.52N, 68.77W	4604	119	0
	OPAL (OP)	2007-2022	79.99N, 85.94W	2223	34	0
	Iqaluit (IQ)	2008-2020	63.75N, 68.54W	1190	60	0
North Africa	Cape_Verde (CV)	1994-2022	16.73N, 22.94W	6020	174	1912
	Dakar (DK)	1996-2020	14.39N, 16.96W	9674	975	3620
	Izana (IZ)	1997-2022	28.31N, 16.50W	5114	0	87
Middle East	Eilat (EI)	2007-2022	29.50N, 34.92E	9290	503	263
	Solar_Village (SV)	1999-2015	24.907N, 46.40E	14278	1839	2234
	Mezaira'a (ME)	2004-2022	23.11N, 53.76E	8679	1672	998
Asia	Dushanbe (DU)	2010-2022	38.55N, 68.86E	4939	621	331
	Dalanzadgad (DA)	1997-2022	43.58N,104.42E	3864	10	12

	SACOL(LA)	2006-2013	35.95N,104.14E	3382	317	186
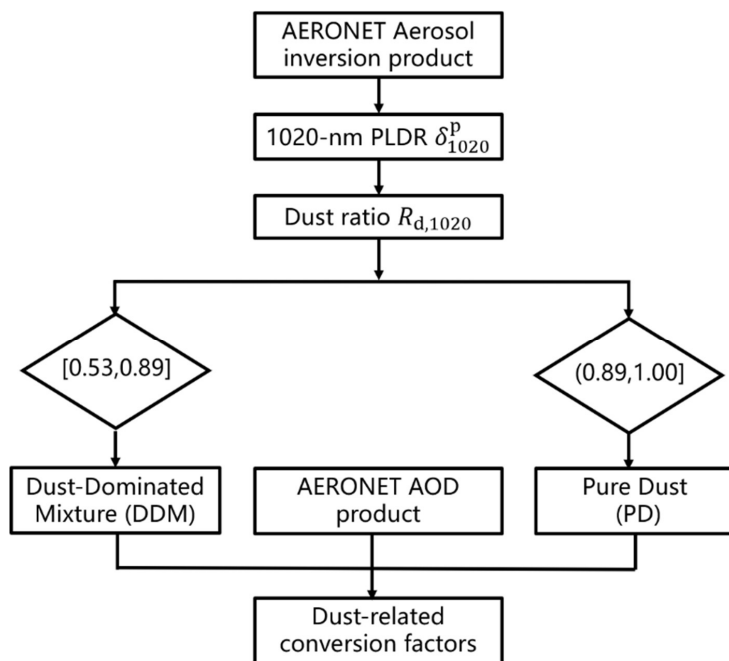
Figure 2: Flow chart for retrieving the dust-related POLIPHON conversion factors.
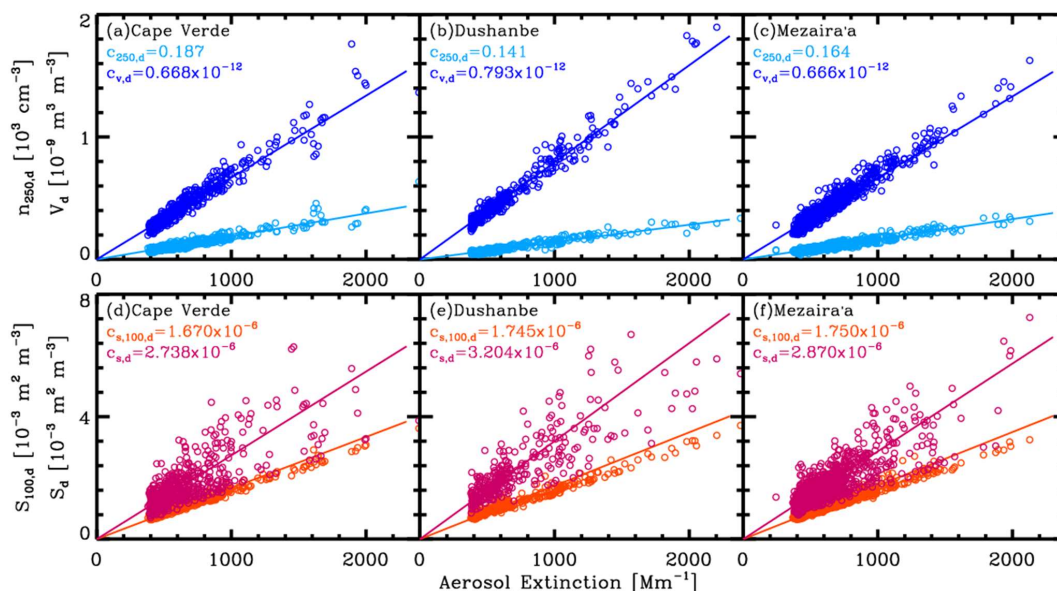
Figure 3: Relationship between aerosol extinction coefficient at 500 nm and large particle (with radius >250 nm) number concentration $n_{250,d}$ and volume concentration v_d, and surface area concentration s_d and $s_{100,d}$ (only considering particles with radius >100 nm) for pure dust at three typical sites, i.e., (a) and (d) for Cape Verde, (b) and (e) for Dushanbe, and (c) and (f) for Merzaira'a. The pure dust data points are selected from the AERONET V3 database (level-2.0 AOD products and level-2.0 aerosol inversions) using the threshold of particle linear depolarization ratio derived with the method given by Shin et al. (2019). The corresponding dust-related conversion factors $c_{v,d}$, $c_{250,d}$, $c_{s,d}$ and $c_{s,100,d}$ are also given, respectively.

Table 3. POLIPHON dust-related conversion factors $c_{v,d}$ (10^{-12} Mm), $c_{250,d}$ (Mm cm^{-3}), $c_{s,d}$ (10^{-12} Mm m^2 cm^{-3}) and $c_{s,100,d}$ (10^{-12} Mm m^2 cm^{-3}) for DDM+PD and only PD, respectively. The respective standard deviations are also provided. The sites are classified into three regional clusters, including North Africa, the Middle East, and Asia.

	Site	$C_{v,d}$ (10^{-12}Mm)		$C_{250,d}$ (Mm cm^{-3})		$C_{s,d}$ (10^{-12}Mm m^{2}cm^{-3})		$C_{s,100,d}$ (10^{-12}Mm m^{2}cm^{-3})	
		DDM+PD	PD	DDM+PD	PD	DDM+PD	PD	DDM+PD	PD
North Africa	CV	0.67±0.07	0.67±0.07	0.19±0.03	0.19±0.03	2.78±0.72	2.73±0.69	1.71±0.19	1.67±0.12
	DK	0.66±0.09	0.67±0.08	0.18±0.03	0.18±0.03	2.96±0.81	2.83±0.72	1.80±0.29	1.71±0.17
	IZ	0.63±0.05	0.63±0.05	0.20±0.02	0.20±0.02	2.32±0.43	2.32±0.43	1.58±0.08	1.58±0.08
Middle East	EI	0.60±0.11	0.65±0.08	0.16±0.03	0.18±0.03	3.02±0.97	2.37±0.54	2.20±0.71	1.63±0.12
	SV	0.71±0.09	0.74±0.07	0.15±0.02	0.16±0.02	2.86±0.68	2.75±0.64	1.81±0.32	1.65±0.14
	ME	0.64±0.09	0.67±0.08	0.16±0.03	0.16±0.02	3.11±0.70	2.87±0.59	2.04±0.44	1.75±0.16
Asia	DU	0.78±0.10	0.79±0.07	0.13±0.03	0.14±0.02	3.29±0.70	3.20±0.70	1.97±0.32	1.74±0.18
	DA	0.66±0.16	0.84±0.33	0.17±0.04	0.18±0.04	3.26±1.31	3.17±1.42	2.22±0.78	2.03±0.79
	LA	0.66±0.12	0.73±0.10	0.17±0.04	0.16±0.02	3.37±0.77	3.30±0.77	1.86±0.24	1.67±0.13

660
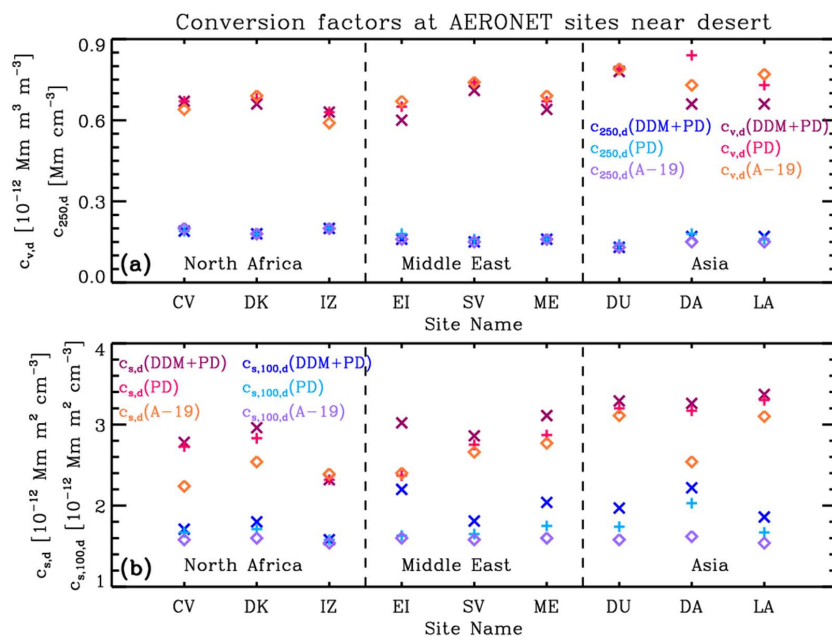
Figure 4: Intercomparison of dust-related conversion factors at nine sites (as shown in Table 2) near the deserts (a) $c_{v,d}$ and $c_{250,d}$, and (b) $c_{s,d}$ and $c_{s,100,d}$ calculated with the dust (both PD+DDM and PD) data selection scheme (based on particle linear depolarization ratio) in this study with those derived with the constraints of Ångström exponent for the 440–870 nm wavelength range $AE_{440\text{-}870}$ <0.3 and aerosol optical depth at 532 nm AOD_{532} >0.1 given by Ansmann et al. (2019b) (denoted as 'A-19').
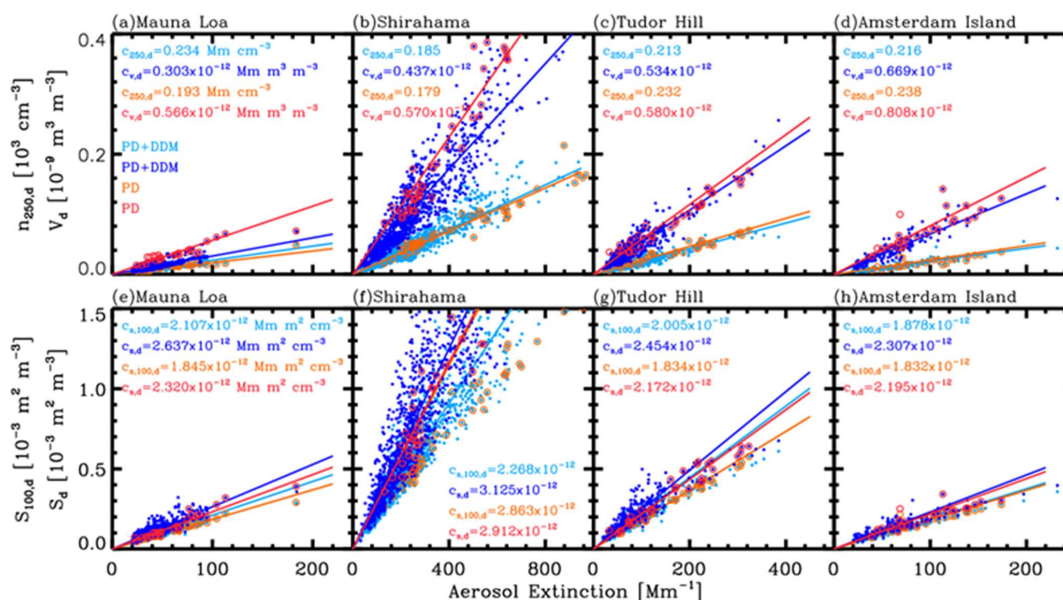
Figure 5: Relationship between the aerosol extinction coefficient at 500 nm and large particle (radius >250 nm)
number concentration $n_{250,d}$ and volume concentration v_d, and surface area concentration s_d and $s_{100,d}$ (radius >100
nm) for DDM+PD and PD at four typical ocean and coast sites, i.e., (a) and (d) for Mauna Loa, (b) and (f) for
Shirahama, (c) and (g) for Tudor Hill, and (d) and (h) for Amsterdam Island. The PD and DDM data points are
selected from the AERONET Version 3 database (level-2.0 AOD products and level-1.5 aerosol inversion products)
using the dust ratio threshold derived with the method given by Shin et al. (2019). The corresponding values of dust-
related conversion factors $c_{v,d}$, $c_{250,d}$, $c_{s,d}$, and $c_{s,100,d}$ are also given, respectively.

Table 4. POLIPHON dust-related conversion factors $c_{v,d}$ (in 10^{-12} Mm), $c_{250,d}$ (in Mm cm^{-3}), $c_{s,d}$ (in 10^{-12} Mm m^2 cm^{-3}) and $c_{s,100,d}$ (in 10^{-12} Mm m^2 cm^{-3}) for DDM (dust-dominated mixture) +PD (pure dust) and only PD based on the AERONET data analysis. The respective standard deviations are also provided. The sites are classified into five regional clusters, including the Pacific, Pacific coast, Atlantic, Indian Ocean, and Arctic Ocean.

680

	Site	$C_{v,d}$ (10^{-12}Mm)		$C_{250,d}$ (Mm cm^{-3})		$C_{s,d}$ (10^{-12}Mm m^{2}cm^{-3})		$C_{s,100,d}$ (10^{-12}Mm m^{2}cm^{-3})	
		DDM+PD	PD	DDM+PD	PD	DDM+PD	PD	DDM+PD	PD
Pacific	TA	0.60±0.14	-	0.17±0.03	-	2.43±0.49	-	1.84±0.22	-
	NR	0.67±0.16	0.73±0.16	0.19±0.04	0.23±0.09	2.07±0.38	1.93±0.40	1.71±0.23	1.71±0.35
	MI	0.57±0.15	0.66±0.16	0.21±0.04	0.19±0.03	2.27±0.38	2.01±0.27	1.88±0.24	1.71±0.19
	AS	0.62±0.15	0.79±0.09	0.19±0.04	0.18±0.06	2.26±0.45	2.28±0.53	1.83±0.25	1.87±0.37
	GA	0.61±0.14	-	0.23±0.05	-	2.01±0.38	-	1.74±0.25	-
	ML	0.31±0.10	0.57±0.11	0.24±0.05	0.19±0.03	2.72±0.61	2.32±0.61	2.19±0.38	1.85±0.16
Pacific Coast	HU	0.44±0.13	-	0.17±0.04	-	3.22±0.81	-	2.18±0.33	-
	OS	0.49±0.10	0.67±0.18	0.20±0.04	0.17±0.03	3.32±0.83	3.43±0.89	2.30±0.43	2.02±0.42
	SH	0.44±0.12	0.57±0.10	0.19±0.04	0.18±0.02	3.13±0.89	2.91±0.69	2.27±0.50	1.82±0.20
	SI	0.31±0.07	-	0.21±0.04	-	2.68±0.62	-	2.04±0.29	-
	TR	0.44±0.12	0.58±0.09	0.21±0.04	0.20±0.04	2.40±0.46	2.33±0.60	1.97±0.27	1.97±0.55
Atlantic	AG	0.52±0.13	0.58±0.08	0.22±0.04	0.22±0.03	2.29±0.40	2.23±0.34	1.84±0.25	1.71±0.17
	TH	0.53±0.14	0.58±0.14	0.21±0.06	0.23±0.04	2.45±0.53	2.17±0.35	2.00±0.32	1.83±0.20
	SH	0.49±0.12	-	0.21±0.05	-	2.74±0.86	-	2.14±0.51	-
Indian Ocean	MG	0.53±0.16	-	0.21±0.05	-	2.19±0.31	-	1.83±0.20	-
	AI	0.67±0.16	0.81±0.20	0.23±0.07	0.21±0.06	2.35±0.53	2.20±0.47	1.92±0.36	1.83±0.34
Arctic Ocean	NA	0.31±0.05	-	0.21±0.04	-	2.96±0.69	-	2.23±0.34	-
	TL	0.27±0.04	-	0.22±0.04	-	2.71±0.42	-	2.22±0.29	-
	OP	0.27±0.06	-	0.23±0.04	-	2.50±0.27	-	2.08±0.19	-
	IQ	0.28±0.06	-	0.26±0.04	-	2.75±0.46	-	2.31±0.29	-
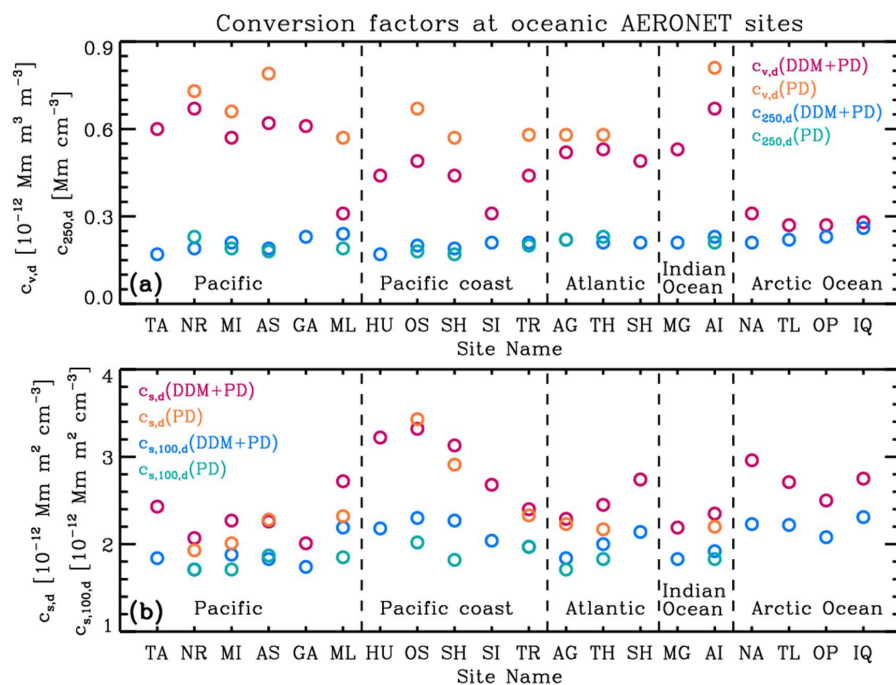
**Figure 6: Dust-related conversion factors at 20 oceanic and coast sites (a) $c_{v,d}$ and $c_{250,d}$, and (b) $c_{s,d}$ and $c_{s,100,d}$
calculated by considering PD and DDM+PD datasets, respectively.**
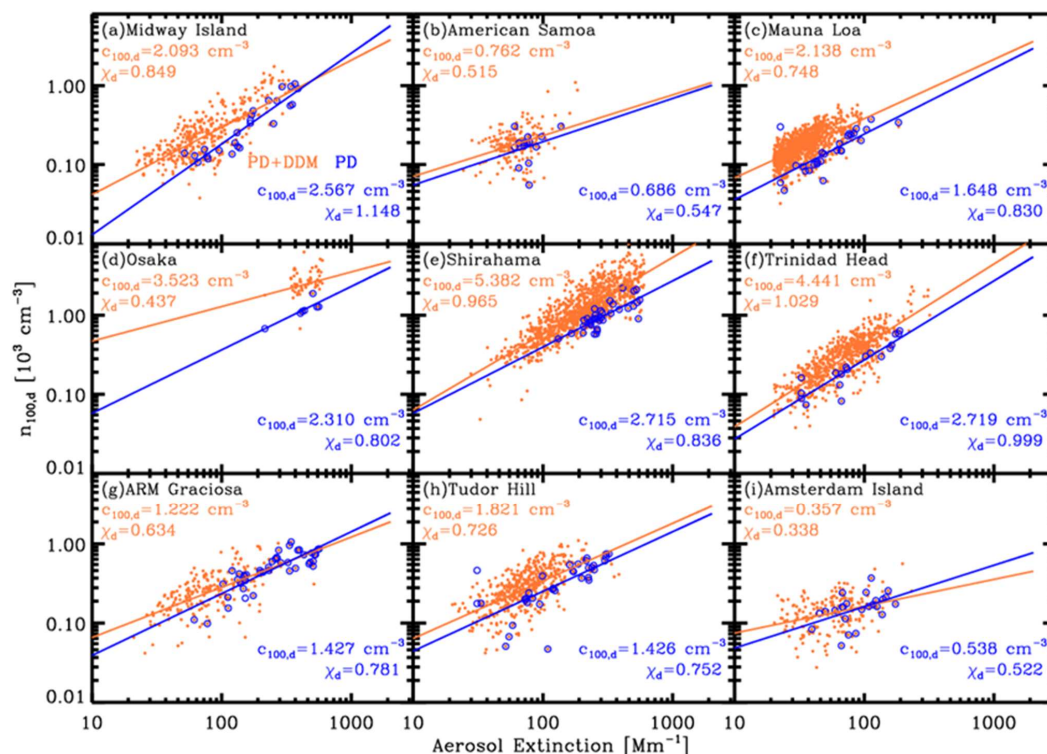
Figure 7: Relationship between aerosol extinction coefficient at 500 nm and aerosol particle number concentration $n_{100,d}$ **(radius >100 nm) for DDM+PD (in orange) and PD (in blue) at nine ocean and coast sites, i.e., (a) Midway Island, (b) American Samoa, (c) Mauna Loa, (d) Osaka, (e) Shirahama, (f) Trinidad Head, (g) ARM Graciosa, (h) Tudor Hill, and (i) Amsterdam Island. The PD and DDM data points are selected from the AERONET Version 3 database (level-2.0 AOD products and level-1.5 aerosol inversion products) using the dust ratio threshold derived with the method given by Shin et al. (2019). The corresponding dust-related conversion factors** $c_{100,d}$ **and** χ_d **are also provided.**

Table 5. POLIPHON dust-related conversion factors $c_{100,d}$ (in cm^{-3} for α_d=1 Mm^{-1}) and χ_d for DDM (dust-dominated mixture) +PD (pure dust) and only PD based on the AERONET data analysis. The sites are classified into 5 clusters, including the Pacific, Pacific coast, Atlantic, Indian Ocean, and Arctic Ocean.

Level 2.0	Site	$C_{100,d}$ (cm^{-3} for α_d=1 Mm^{-1})		χ_d	
		DDM+PD	PD	DDM+PD	PD
Pacific	Tahiti (TA)	2.73	-	0.91	-
	Nauru (NR)	-	-	-	-
	Midway_Island (MI)	2.09	2.92	0.85	1.24
	American_Samoa (AS)	0.76	0.69	0.52	0.55
	Guam (GA)	-	-	-	-
	Mauna_Loa (ML)	2.14	1.65	0.75	0.83
Pacific coast	Hokkaido_University (HU)	5.52	-	1.00	-
	Osaka (OS)	3.52	2.31	0.44	0.80
	Shirahama (SH)	5.38	2.72	0.97	0.83
	Saturn_Island (SI)	3.95	-	0.90	-
	Trinidad_Head (TR)	4.44	2.72	1.03	1.00
Atlantic	ARM_Graciosa (AG)	1.21	1.43	0.63	0.78
	Tudor_Hill (TH)	1.82	1.43	0.73	0.75
	St_Helena (SH)	1.95	-	0.70	-
Indian Ocean	Maldives_Gan (MG)	2.71	-	0.91	-
	Amsterdam_Island (AI)	-	0.54	-	0.52
Arctic Ocean	Narsarsuaq (NA)	3.80	-	0.86	-
	Thule (TL)	3.75	-	0.83	-
	OPAL (OP)	2.05	-	0.62	-
	Iqaluit (IQ)	3.57	-	0.80	-

700
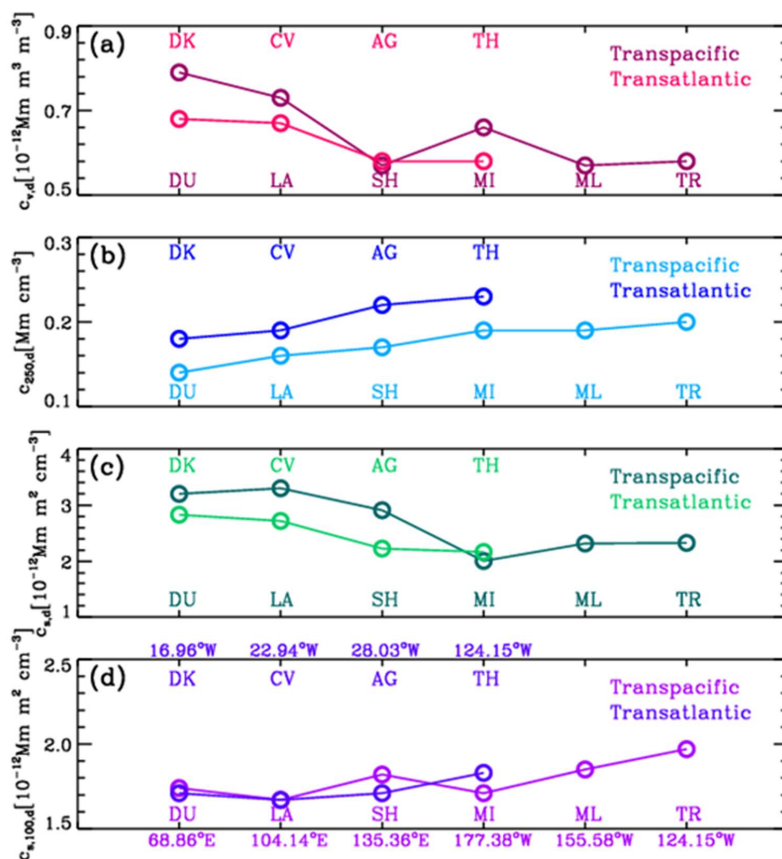
Figure 8: Variations in conversion factors (a) $c_{v,d}$, (b) $c_{250,d}$, (c), $c_{s,d}$ and (d) $c_{s,100,d}$ along transoceanic dust transport paths, including a transpacific path from Asian dust sources to the west coast of North America and a transatlantic path from the Saharan Desert (North Africa) to the east coast of North America. The longitudes of the sites are also shown.

705